Reynolds Number Scaling of Flow in a Rushton Turbine Stirred Tank. Part I – Mean Flow, Circular Jet and Tip Vortex Scaling

H.S. Yoon[1], D.F. Hill[2], S. Balachandar[3*], R.J. Adrian[3], M.Y. Ha[1]

[1]School of Mechanical Engineering, San 30 Chang Jeon Dong, Pusan National University, S. Korea

[2]Department of Civil & Environmental Engineering, 212 Sackett Building, Pennsylvania State University, University Park, PA, 16802

[3]Department of Theoretical & Applied Mechanics, 216 Talbot Lab, University of Illinois, Urbana, IL, 61801

Abstract

We consider scaling of flow within a stirred tank with increasing Reynolds number. Experimental results obtained from two different tanks of diameter 152.5 and 292.1 mm, with a Rushton turbine operating at a wide range of rotational speeds stirring the fluid, are considered. The Reynolds number ranges from 4,000 to about 78,000. Phase-locked stereoscopic PIV measurements on three different vertical planes close to the impeller give phase-averaged mean flow on a cylindrical surface around the impeller. The scaling of q-averaged and plane-averaged radial, circumferential and axial mean velocity components is first explored. A theoretical model for the impeller-induced flow is used to extract the strength and size of the three dominant elements of the mean flow, namely the circumferential flow, the jet flow and the pairs of tip vortices. The scaling of these parameters with Reynolds number for the two different tanks is then obtained. The plane-averaged mean velocity scales with the blade tip velocity above a Reynolds number of about 15,000. However, parameters associated with the jet and tip vortices do not become Reynolds number independence until Re exceeds about 10^5. The results for the two tanks exhibit similar Reynolds number dependence, however, a perfect collapse is not observed, suggesting a sensitive dependence of the mean flow to the finer details of the impeller.

Keywords: Rushton turbine, turbulence, mixing, scaling, particle image velocimetry

* Corresponding Author, Phone: 217-244-4371, Fax: 217-244-9090, email: s-bala@uiuc.edu.

1. Introduction

Scaling of flow and mixing within a stirred tank reactor is of significant practical importance. For lack of a satisfactory understanding, the design of production-scale stirred tanks often evolves through a number of stages that iterate between laboratory experiments and pilot plants, a time-consuming and expensive step-by-step scale-up process. Part of the difficulty is that mean flow and turbulence quantities, such as rms fluctuation and dissipation, often scale differently with increasing tank size and operating speed. As a result the scaling of mixing within the tank can be complex.

Previous experimental investigations have considered flow and mixing inside stirred tanks of varying size operating over a range of speeds and, thus, have addressed, directly or indirectly, the scaling of mean and turbulence quantities with Reynolds number[1-13]. These studies together cover a wide range of Reynolds number from 10 to 1.2×10^5, where Reynolds number is defined in terms of impeller blade-tip diameter, D, and the number of blade rotations per second, N, as $\mathrm{Re} = ND^2/n$ (n is the kinematic viscosity of the fluid). However, the range of Re considered in each investigation is limited. At higher Reynolds numbers relevant to turbulent flow, the overall time-averaged mean flow and rms turbulent fluctuations appear to scale with the impeller blade-tip velocity.

Costes and Couderc[5,6] have addressed the problem of scaling of mean flow and turbulence using two different sized tanks over three different Reynolds numbers. Their results suggest that velocity statistics such as, mean, rms, spectra and autocorrelation scale with the blade-tip velocity. However, higher order turbulence statistics, such as dissipation, do not show complete collapse when scaled appropriately in terms of impeller diameter and rotation rate. The results of Stoots and Calabrese[9] on deformation rate over a Reynolds number range of 29,200 to 45,800, however, show a reasonable Reynolds number independence when nondimensionalized by the inverse time scale.

Molen and Van Maanen[3] emphasized the importance of blade-tip trailing vortices. They pointed out that the time-averaged flow in the laboratory frame of reference (as measured by a fixed probe) averages out the influence of tip vortices as they sweep past the probe along with the blades. The resulting time-averaged mean flow was observed to scale well with the blade-tip velocity. The effect of tip vortex pairs was carefully isolated through phase-average, and the tip vortex strength did not scale perfectly with blade-tip velocity. Some dependence on tank size was observed. Van Riet and Smith[2] also investigated the scaling of blade-tip vortices over a wide Reynolds number range of 300 to 90,000. The vortex trajectory was observed to be Reynolds number dependent at lower, transitional Reynolds numbers, but Reynolds

number independent, within experimental uncertainty, above a Reynolds number of 15,000. Other quantities such as vortex strength, when appropriately scaled, also tended towards Reynolds number independence at higher Reynolds numbers.

In spite of the above efforts the scaling of flow and mixing within a stirred tank with increasing tank size and impeller speed remains not fully understood. In this paper we address the question of scaling with experiments performed in two different tanks with impeller speed varying over Reynolds numbers ranging from 4,000 to 80,000. The two tanks were constructed to be geometrically similar. Both employ a lid at the top of the tank in order to prevent free surface (Froude number) effects. The flow is entirely driven by the rotating impeller and the operational speeds are such that Mach and Rossby numbers are irrelevant. Reynolds number is expected to be the only relevant parameter of the problem. The results for each tank, when appropriately nondimensionalized by the blade tip radius and velocity, show Reynolds number independence with increasing impeller speed at sufficiently high Reynolds number. However, surprisingly the results for the two different tanks do not exhibit a perfect collapse, suggesting sensitive dependence on small differences, especially in the geometric scaling of their impellers.

Stereoscopic particle image velocimetry (PIV) measurements were made on three different vertical planes within the tank. The instantaneous measurements are phase-locked with the blade position and ensemble averaging over many such realizations yields the phase-averaged mean velocity. The measurement on the three planes, which are located close to the impeller swept volume, are interpolated to obtain all three components of the phase-averaged mean velocity on a cylindrical plane of constant radius located just beyond the impeller tip. The velocity on this cylindrical plane is the impeller induced inflow and it can be considered to dictate the flow over the entire tank at large[14]. Thus, here we consider the scaling of velocity measured over this plane as a proxy for scaling of flow over the entire stirred tank.

The phase-averaged mean flow within the tank stirred with a Rushton turbine can be considered to be made up of three different basic flow elements: circumferential flow, a jet flow and pairs of tip vortices associated with the impeller blades. This simple decomposition has been shown to be effective in modeling the impeller induced flow, particularly in the neighborhood of the impeller (see Yoon *et al.*[15]). Here we investigate the scaling of each of these elements individually with increasing tank size and impeller rotation rate. By looking at the scaling of parameters, such as the strength and size of the jet and tip vortex pairs individually, we hope to address the question of mean flow scaling in more detail. In particular, it is of interest to establish the minimum Reynolds number necessary for these parameters to be Reynolds number independent.

Here we will also investigate the scaling of both vorticity and dissipation for the two tanks and in particular, address when they become Reynolds number independent. If the scaling of the mean flow were to be uniform over the entire tank, we expect the scaling of these higher order quantities to follow that of the mean flow. However, it can be anticipated that the Reynolds number independence of the nondimensional vorticity and dissipation will be delayed to much higher Reynolds numbers, since these derivative quantities give more importance to the smaller scales of motion. Thus, the results on the scaling of vorticity and dissipation can be used to interpret the scale-dependence of mean flow scaling.

2. Experimental methodology

2.1 Apparatus

The experiments were an extension of more limited experiments first reported by Hill *et al.*[16]. A schematic overhead view of the set-up for the current stereoscopic particle image velocimetry (PIV) experiments is shown in figure 1. To assess the influence of geometric scaling, two geometrically similar test sections were considered. In both cases, an acrylic, unbaffled[#] circular cylinder was mounted within a slightly larger square tank. The diameters of the two circular tanks were T_1=152.5 cm and T_2=292.1 cm. The cylinder was filled with de-ionized water to a depth equal to its diameter and the volume between the cylindrical and the square tanks was also filled, in order to reduce the optical distortion due to the curved surface. A lid, with a small hole to accommodate the impeller shaft, was placed on top of the liquid. The purpose of the lid was to suppress the free-surface displacement, which becomes significant otherwise at higher speeds of impeller rotation. The tolerances between the shaft, lid, and the cylindrical tank were all very tight.

The two tanks were geometrically similar. The lid on top eliminates any free surface and associated Froude number effect. The flow within the tank is completely determined by the impeller rotation and therefore in the present problem the rotational and velocity scales are not independent (Rossby number becomes irrelevant). Furthermore, the velocities considered are quite low that Mach number effect can be ignored. Thus dynamic similarity between the two tanks could be achieved by simply matching the Reynolds numbers. However, some subtle differences in the impellers of the two different arrangements

[#] The use of baffles is a practical means by which to impede the rotation of the fluid. However, one purpose of these experiments was to obtain detailed data for comparison to CFD results, so the simple baffle-free geometry was chosen.

must be noted. The Rushton impeller for the small tank was supplied by Lightnin, Inc., and the impeller for the large tank was custom made by Proprmix, Inc. Figure 1 also shows the detailed sketch of the impeller geometry with the corresponding measurements for the two tanks. While the diameter of the impeller, blade length, blade height and diamter of the disk were geometrically scaled, the blade thickness, disk thickness, sleeve diameter were not perfectly scaled between the small and large tanks. The ramifications of these seemingly minor differences will be discussed later.

The Rushton turbine was mounted at mid-depth along the axis of the cylinder. The shaft extends through the impeller to the bottom of the tank, where it was held in place by a small nylon sleeve bearing. The bearing eliminated `wobble' of the impeller. Detailed views of the experimental tank and impeller are shown in figure 2. Two different Lightnin Labmaster mixers drove the impellers: the first with a speed range of 50-1,800 rpm and the second with a speed range of 20-550 rpm. Details, such as the mounting of the impeller, position of the top lid, etc., for the two tanks are maintained geometrically similar.

The flow was seeded with 8-micron particles from Potters Industries. New-Wave Nd:Yag lasers, operating at ~50 mJ/pulse, illuminated the flow with a light sheet approximately 1 mm thick. Two TSI PIVCAM 10-30 CCD cameras (1K×1K resolution), equipped with Nikon AF Micro Nikkor 60 mm lenses, acquired images of the illuminated particles. The included angle between the angularly offset cameras was roughly 45^0. Scheimpflug lens mounts were used to reduce the required depth of field and to improve focusing over the field of view. A TSI Laser Pulse Synchronizer and a PC equipped with TSI Stereo Insight software completed the image acquisition package.

2.2 Experimental procedure

Because of the lid, the only upper bounds on impeller speed were those placed by the power and speed limits of the mixers. As a result, it was possible to cover Reynolds numbers ranging from 4000 to 80000. Table 1 details the experimental dimensions for both tanks.

As indicated in figure 2, data were obtained on three vertical planes located very close to the tips of the impeller blades. An optical encoder, focused on the impeller shaft, was used to trigger acquisition such that the impeller blades were in the position shown for each realization. For the small tank experiments, these planes were located at distances of 23.22, 25.13, and 27.67 mm from the impeller shaft. For the large tank experiments, these planes were located at distances of 45.12, 48.77, and 53.64 mm. For each combination of impeller speed and acquisition plane, an ensemble of 500 realizations was obtained.

The raw images from the left and right cameras were individually interrogated and then validated. Finally, the two two-dimensional vector fields were combined, using a mapping determined by calibration,

into a single three-component velocity vector field on a planar surface. The individual data sets were first ensemble averaged to yield a mean velocity field[¶]. The mean velocity fields on the three vertical planes for a given rotational speed were then interpolated, using a second-order fit, onto a 60^0 segment of a cylindrical shell of radius R, as illustrated in figure 2. Finally, the Cartesian velocity components were rotated into polar cylindrical coordinates, yielding radial, circumferential and axial velocity components, $< u_r >, < u_q >$ and $< u_z >$, on the curved cylindrical plane, ie., for r=1.06, $0 \le q \le 60^o$ and $-0.6 \le z \le 0.6$ (see figure 2 for coordinate definition). Here angle brackets indicate an average over the ensemble. Note that here and in what follows all lengths are nondimensionalized by the blade tip radius ($D/2$) and the velocities have been nondimensionalized by the blade-tip velocity ($p\,ND$).

3. Results

3.1 Mean flow scaling

The mean flow ensemble-averaged over all the realizations ($< u_r >, < u_q >, < u_z >$) and interpolated onto the cylindrical surface is shown in figure 3 for the small tank at the lowest rotation speed, corresponding to Re=4,300. In figure 3 frame (a) shows the in-plane velocity vector plot and frame (b) shows the out-of-plane (radial) velocity contours. Only a 60^0 sector is shown, and the view is limited to the top half of the tank with the region below the center-plane obtained by symmetry. The q-dependence of the flow field is due to the presence of the tip vortices, whose impact is most evident in the figure around q=$18^0 \pm 1^0$ and $z \approx 0.1 \pm 0.1$. The tip vortex pair cuts the cylindrical plane at an angle, and its sense of rotation is such that it enhances the radial velocity due to the jet at the midplane (z=0), but opposes the jet sufficiently away from the mid-plane. In fact, the negative radial velocity and its localized peak around q=18^0 and $z \approx 0.2$ is a clear signature of the tip vortex. Figure 3 (frames c and d) shows the mean flow for the small tank corresponding to a higher Reynolds number of 63,180. Although the in-plane and radial velocity components are qualitatively similar to the low Reynolds number case, measurable quantitative differences can be observed, indicating a Reynolds number effect. For example, the peak (positive and negative) radial velocities are somewhat lower at the higher Reynolds number than at the lower Re. Figure 4 shows the mean flow results for the large tank at Re= 4,229 and 62,646. They are, again, qualitatively

[¶] With regards to the present data, the term "mean flow" denotes phase-averaged flow obtained from the ensemble average of the phase-locked measurement. It is therefore dependent on all three coordinates. Any further

comparable to those shown in figure 3. Some differences can be observed, in particular, the signature of the tip vortex moves closer to the blade (smaller values of q), suggesting some difference in the tip vortex location and orientation. Again, a comparison of figure 4b with 4d reveals that the intensity of radial velocity appears to decrease with increasing angular velocity of the blade. However, for about the same Reynolds number the radial velocity for the large tank is somewhat stronger than the small tank.

The normalized mean radial, circumferential and axial velocities averaged over q, $\overline{< u_r >}, \overline{< u_q >}, \overline{< u_z >}$, (overbar indicates q-average) are shown in figure 5 for the small tank. Upon q-average the effect of tip vortex pairs gets averaged, and the contribution to the mean flow from the jet stands out, being clearly evident as the rapid increase in the radial velocity as the midplane is approached. The weak negative peak in the radial velocity around z=0.2 is due to the tip vortex pair, but the asymptotic negative radial velocity approached for large z is due to the broad return flow back towards the impeller region. The jet has a strong circumferential component oriented in the direction of blade rotation (note that q is measured in the direction opposite to blade rotation). At this radial location (r=1.06) the radial component of the jet is larger than the circumferential component. As can be seen in figure 5b, as z increases the circumferential velocity approaches a constant value, suggesting a background circumferential flow, which is only weakly dependent on z. The magnitude of the radial velocity steadily decreases with increasing Reynolds number, while the magnitude of circumferential velocity increases with Re. However, a tendency towards Reynolds number independence for these normalized velocity profiles is observed with increasing Reynolds number. The axial velocity component is much weaker in magnitude, and it arises from the jet-induced entrainment and also from the large tank-wide circulation. Although the variation with increasing Re is not monotonic, a tendency towards Reynolds number independence can be observed here, as well.

The above results for the small tank compare favorably with those for the large tank shown in figure 6. The jet amplitude for the large tank appears to be slightly stronger than that for the small tank. Apart from this difference, the comparisons of all three components of velocity in figures 6 and 5 are quite good, especially in the high Reynolds number range. This observation, along with the differences observed earlier between figures 3 and 4, suggests that the tip vortex pairs depend on tank size. This may be due to the critical dependence of tip vortices on the impeller geometry and the small difference in the impellers

---

space average of the mean flow will be explicitly stated in what follws.

between the two tanks may be contributing to this small, but noticeable, difference in the tip vortex signatures.

Figure 7a shows the normalized mean radial, circumferential and axial velocities averaged over the entire q-z plane, $\overline{\overline{< u_r >}}, \overline{\overline{< u_q >}}, \overline{\overline{< u_z >}}$, (the double overbar indicates a planar average) as a function of Re for the two different tank sizes. Above a Reynolds number of about 15,000 the results for all three components of velocity show very little variation. The average velocities in the two different tanks are in reasonable agreement as Re increases, except for the radial component of velocity. The scaling of the maximum value of $< u_r >$, $< u_q >$ and $< u_z >$, maximum over the q-z plane, is shown in figure 7b as a function of Re for the two different tank sizes. Even the axial component of velocity shows a weak dependence on tank size in its asymptotic value appropriate at large Re. These differences in the results for the two tanks must have their origin in the subtle departures from a perfect geometric scaling of the two impellers.

Here, it should be pointed out that in some of the earlier efforts[3,10] the comparison of different tank sizes is performed while maintaining the volume averaged mean dissipation rate to be the same. Since dissipation scales as $N^3 D^2$, it can be expected to go as Re^3 in a fixed tank with increasing blade tip velocity, or as D^{-4} with increasing tank size for a fixed Re. Fixed dissipation rate implies that with increasing tank size one must consider increasing blade tip velocity such that $\mathrm{Re} \propto D^{4/3}$. The good degree of Reynolds number independence exhibited in both the tanks in figure 7 suggests that the lack of perfect collapse between the two tanks will persist even when compared on the basis of constant volume averaged mean dissipation rate.

It is interesting to note that for the large tank at the lowest Re considered the maximum circumferential velocity exceeds the blade tip velocity (possibly due to the tip vortex influence). With increasing Reynolds number, however, the magnitude of peak circumferential velocity is reduced below the blade tip velocity. While the peak radial velocity remains comparable to the peak circumferential velocity, in terms of the surface-averaged mean, the radial velocity is an order of magnitude weaker than the circumferential component. This is to be expected, since a radial return flow is required to satisfy continuity, and as can be seen in figures 5 and 6, even a short distance away from the impeller (for $|z| > 0.2$) the radial velocity is negative.

3.2 Decomposition of mean flow

The theoretical model presented in Yoon *et al.*[15], considered the impeller-induced phase-averaged mean flow as a superposition of a circumferential flow, a circular jet and a pair of tip vortices associated with each impeller blade. Their superposition for the mean flow, in a frame of reference rotating with the blade, can be expressed as:

$$\mathbf{u}(r,\theta,z) = \mathbf{u}_{\mathrm{c}}(r,z) + \mathbf{u}_{\mathrm{jet}}(r,z) + \mathbf{u}_{\mathrm{vort}}(r,\theta,z) \tag{1}$$

where $\mathbf{u}_{\mathrm{c}}$ is a purely circumferential flow. Its strongest variation is along the radial direction, and it is only weakly dependent on z. In the laboratory frame of reference the time averaged flow is axisymmetric as the effect of the impeller blades gets averaged out and remains invariant to θ. The effect of the impeller blades and the associated tip vortices can be better accounted for in the mean flow in a frame of reference that rotates with the blades. In the rotating frame, the blades remain fixed in position and the time averaged mean flow is periodic over the 60^0 sector between the blades. Thus, the above superposition in the rotating frame of reference allows for the description of a complex impeller-induced flow, with all three (radial, circumferential and axial) components of velocity strongly dependent on all three coordinate directions.

In the case of a Rushton turbine the jet flow slowly changes direction from a circumferential direction to a more radial direction with increasing radial distance from the axis[4,17,18]. Thin shear layer theory can be applied and an approximate self-similar solution can be obtained for the jet (see Yoon *et al.*[15]). At any radial distance, r, from the axis of the tank the self-similar jet is directed at an angle $\theta_{\mathrm{jet}} = \cos^{-1}\left(\sqrt{r^2 - a^2}\,/\,r\right)$ to the radial direction and the jet velocity along this direction is given by

$$u_{\mathrm{jet}} = \frac{A}{r^{1/2}(r^2 - a^2)^{1/4}}\left\{1 - \tanh^2\left(\frac{s\,z}{\sqrt{r^2 - a^2}}\right)\right\} \tag{2}$$

The jet flow is fully characterized by three parameters: A - a measure of the jet momentum, $1/\sigma$ - a measure of the jet thickness and a - the virtual origin.

The tip vortices are generated from the roll-up of the shear layers as flow accelerates around the rotating impellers[3,9,19]. The tip vortices are at their peak strength close to the impellers and weaken as they extend radially out into the tank. The backbone of the tip vortex pair is curved backwards in the circumferential direction opposite to the direction of rotation. The tip vortices remain coherent, and as shown in the recent large eddy simulations,[14] at any instant in time they extend over 180^0 along the

circumferential direction. While their head remains anchored behind the rotating blades, their tail oscillates in position over time as they extend into the tank. Upon time averaging, a tip vortex pair's extent into the tank is somewhat reduced to about 60^0 along the circumferential direction. Yoon *et al.*[15] observed that the strength and size of the average tip vortex pair changes along its backbone.

The full details of the tip vortex pair along its entire backbone cannot be obtained from the present PIV measurements. But, velocity fields such as those shown in figures 3 and 4 can be used to characterize the tip vortex pair as it cuts through the cylindrical plane $r\approx1.06$. On this plane the location of tip vortex pair is characterized by q_v, the angle between the vortex center and the nearest blade and $\pm z_v$, the axial location of the vortex centers from the midplane. The vortex backbone cuts the cylindrical plane, $r\approx1.06$, at an oblique angle and thus the local orientation of the vortex pair is additionally characterized by the angle, f_v, between the backbone and the local radial direction. To good approximation the vortex pair can be taken to be viscous vortices. Therefore the azimuthal velocity (different from circumferential or q component of velocity) in the neighborhood of any of the vortex on a plane normal to the vortex backbone can be expressed as

$$u_{\text{azim}} = \frac{\Gamma}{x}\left[1-\exp\left(-dx^2\right)\right] \tag{3}$$

where, x is the normal (shortest) distance from the vortex backbone to the point at which the velocity is evaluated. The other two parameters that characterize the vortex are: Γ, the strength (or circulation) of the vortex and, $1/\sqrt{d}$, the vortex core diameter. The above five parameters completely characterize the effect of the tip vortices, at least in the neighborhood of the impeller.

3.3 Tip vortex scaling

The influence of circumferential flow and circular jet can be subtracted from the experimental measurements to isolate the contribution from the tip vortex pairs. Following a procedure similar to that in Yoon *et al*[15] we extract the parameters associated with the tip vortex pair that yield the best match to the experimental measurements. Table 2 shows the location of the tip vortex centers on the cylindrical plane ($r\approx1.06$) in terms of their axial position ($\pm z_v$) with respect to the midplane and circumferential (q_v) position measured with respect to the nearest blade in the direction opposite to the direction of impeller rotation. In nondimensional terms, the axial location of the vortex center about the midplane remains nearly independent of Reynolds number and shows a slight increase with the size of the tank. The nondimensional

total height of the blade is 0.4; thus the vortices are located roughly halfway between the center plane and the top or bottom edge of the blade. The circumferential location of the vortex center also does not show a strong dependence on Reynolds number, however, with increasing tank size the vortex center is observed to move closer to the blade.

Van Riet and Smith[2] observed the curvature of the vortex trajectory and as a result the circumferential location of the vortex, q_v, to decrease initially with Reynolds number. However, for Re greater than about 5000 they observed the vortex trajectory to be nearly Reynolds number independent within the uncertainties of the experimental measurement. The Reynolds number range for present investigation is in general larger than 5,000. Nevertheless, the slight increase in q_v with increasing Reynolds number seen in table 2, opposes the trend observed by Van Riet and Smith[2].

Also shown in table 2 is the angle, f_v, the vortex backbone makes with the radial direction at the point where it intersects the cylindrical plane ($r \approx 1.06$). For both the small and large tanks the angle, f_v, shows a slight increase with increasing Reynolds number, indicating a more circumferential orientation for the tip vortex trajectory at higher Re. This result is consistent with the observed slight increase in q_v with Reynolds number. At lower Reynolds numbers the tip vortex backbone is directed closer to the radial direction in the large tank than in the small tank. However, as Re increases to larger values, for both tanks f_v appears to asymptote to an angle of about 60^0. Within the impeller swept volume (for $r<1$) on the leeward side of the rotating blades the tip vortex pairs lie parallel to the blade and have a near radial orientation. Within a short distance away from the blade tip the tip vortices sharply curve backwards. As can be seen from table 2, for all cases considered f_v is noticeably higher than 45^0, indicating a more circumferential local orientation for the vortex backbone.

Figures 8a shows a plot of the nondimensional vortex strength as a function of Re for the two different tanks considered (nondimensionalized by $pND^2/2$). The nondimensional vortex strength decreases with increasing Re, with the rate of decrease higher at lower Re. A tendency towards Reynolds number independence can be inferred, although even for the highest Reynolds number considered this asymptotic state is not yet attained for the large tank. From the figure it appears that for both tanks an asymptotic value of about 0.017 may be appropriate for Re greater than about 10^5. The above scaling indicates that the relative importance of the vortex pair is higher at lower Reynolds number and levels off at higher Reynolds numbers. The observed dependence of nondimensional vortex strength with tank size may be due to the subtle differences in the actual impellers employed for the small and large tanks.

Interestingly the measurements of Molen and van Maanen[3] also shows a dependence of tip vortices on tank size.

The measure of vortex size, $1/\sqrt{d}$, is shown in figure 8b. For the small tank the nondimensional size decreases slightly from a value of about 0.085 at lower Re to an asymptotic value of about 0.07 with increasing Re. The relative size of the vortex is somewhat small for the large tank. With increasing Re the asymptotic value of $1/\sqrt{d}$ for the large tank is about 0.055. The large tank is twice bigger than the small tank, and therefore in dimensional terms the vortex size for the large tank is only about factor 1.5 bigger than that for the small tank.

3.4 Scaling of the circular jet

Figure 9a shows the nondimensional jet momentum parameter, *A*, (nondimensionalized by $\rho ND^2/2$) for varying Reynolds number for the two different tanks. For the small tank an asymptotic constant value of about 0.165 is reached for Re greater than about 45,000. For the large tank a complete Reynolds number independence is not observed even for the largest Reynolds numbers considered. However, a tendency towards Reynolds number independence may develop at Re exceeding 75,000. The strength of the jet in nondimensional terms is observed to be somewhat stronger for the large tank and that is consistent with the differences between the two tanks seen in figures 5 and 6.

Figure 9b shows that the inverse jet thickness, s, for the two different tanks exhibits better collapse than the jet momentum. The nondimensional jet thickness decreases with increasing Reynolds number at lower Reynolds numbers, and above a Reynolds number of about 30,000, the jet thickness appears to level off and become nearly independent of Re. The asymptotic value of nondimensional inverse jet thickness for the two tanks is, $s_{asym} \approx 6$. Note that the impeller radius is the length scale used in the nondimensionalization and hence, in dimensional terms, the jet width is about one sixth (0.166) of the impeller radius. This can be compared with the height of the impeller blade, which is approximately 0.4 times the impeller radius.

Figure 9c shows the variation of virtual origin, a, with respect to Re for the two different tanks. A similar trend is exhibited for both tanks with the virtual origin progressively increasing with increasing Reynolds number. The rate of increase is, however, somewhat larger for the large tank. For both tanks a clear asymptotic behavior is not reached even for Reynolds number as large as 75,000.The approach of the virtual origin closer to blade tip (r=1) suggests that as Reynolds number increases the importance of

circumferential component of jet velocity increases at the expense of the radial component, which is again consistent with the velocity profiles shown in figures 5 and 6. However, as pointed out earlier, at the radial location of velocity measurement the radial component of the jet is somewhat stronger than the circumferential component over the entire Reynolds number range considered.

3.5 Scaling of the circumferential flow

At the plane of interpolated experimental mean flow data (at $r \approx 1.06$) the jet is neither completely radial nor purely circumferential. The jet flow has a circumferential component, which for increasing Reynolds number can be inferred to be slightly larger for the large tank than for the small tank (owing to the somewhat larger value of a for the large tank). This contribution alone does not fully account for the measured q-velocity and the circumferential impeller-induced flow, $\mathbf{u}_c$, is defined to account for the balance (Note that $\mathbf{u}_c$ is directed purely in the circumferential diretion). Figures 10a and 10b show the circumferential flow, $\mathbf{u}_c$, as a function of axial location at $r \approx 1.06$ for the varying Reynolds numbers for the two different tanks. Only the region close to the impeller ($z<0.5$), where the measurement is made, is shown. For comparison the blade extends from $-0.2<z<0.2$, while the tank from bottom to top is given by $-3<z<3$.

In the rotating frame of reference the impeller-induced circumferential flow is directed opposite to the direction of blade rotation. The circumferential flow, $\mathbf{u}_c$, is weakly dependent on the axial direction for the small tank and only slightly more dependent in the large tank, close to the impeller blade. A clear Reynolds number dependence occurs in both the tanks. The magnitude of the circumferential flow initially increases with increasing Reynolds number, but, above a Reynolds number of about 45,000 saturation occurs. For the small tank the magnitude of the nondimensional circumferential flow increases from a value of about 0.4 at Re=4,300 to a value of about 0.5 at the higher Reynolds number. For the large tank the magnitude of increases from a value of about 0.44 at Re=4,229 to a value of about 0.5 at the highest Reynolds number considered. Thus, at sufficiently large Reynolds number the circumferential flow scales with the blade-tip velocity.

On the cylindrical surface of interpolated mean velocity the effect of tip vortices is the strongest on the leeward side of the blade (that is for small values of q). On this surface the velocity field at large values of q is dominated by the jet and the circumferential flow. Thus the efficiency of the jet and the circumferential flow models in capturing the measured mean flow variation can be evaluated from the data

at large q. As an example, figure 11a shows the experimental mean radial, circumferential and axial velocity components as a function of z at q=55^0 for the small tank at Re=23,700. The corresponding result for the large tank at Re=23,492 is shown figure 11b. The excellent representation for the circumferential velocity component is due to the fact that the circumferential component, $\mathbf{u}_c$, has been defined to yield the best agreement for large q. Good representation can be observed for the radial velocity, except the model is constrained to approach zero radial velocity with increasing z, while a small negative radial inflow is observed in the experiment for large z for the small tank.. The agreement for the axial velocity is reasonable; however the magnitude of axial velocity is significantly smaller than the other two components. Similar comparison has been made for both the tanks over the entire range of Re.

3.6 Vorticity and dissipation scaling

The measurement of all three components of the mean velocity on three parallel planes allows for accurate evaluation of all components of the mean velocity gradient and thus vorticity and dissipation fields associated with the mean flow. Here we will investigate the scaling of both vorticity and dissipation for the two tanks. The phase-averaged mean radial vorticity can be defined in terms of the mean flow as

$$\langle w_r \rangle = \frac{1}{r}\frac{\partial \langle u_z \rangle}{\partial q} - \frac{\partial \langle u_q \rangle}{\partial z}. \qquad (4)$$

A contour plot of the radial vorticity for the small tank on the cylindrical plane at r≈1.06 is shown in figures 12a and 12b for the two Reynolds numbers Re=4,330 and Re=63,180. The radial vorticity clearly seems to be associated with the tip vortex pair and the location of peak vorticity is close to the tip vortex center. The distribution of vorticity is qualitatively similar for both the Reynolds numbers, however, the extent of vorticity and the peak value are somewhat lower with increasing Reynolds number. The corresponding vorticity fields for the large tank for Re=4,229 and Re=78,308 are shown in frames (c) and (d). The region of significant vorticity is somewhat smaller for the large tank, but the peak vorticity is significantly stronger than that for the small tank, especially at the lower Reynolds number. The difference between the two tanks greatly decreases at the higher Reynolds number. This result is consistent with the tip vortex strengths for the two tanks shown in figure 8a.

The square-root of surface-averaged mean square vorticity, $\sqrt{\overline{\langle w_r \rangle}}$, as a function of Re for the two different tanks is shown in figure 13a and the corresponding trend of the surface maximum radial vorticity is shown in figure 13b. Compared to the mean flow the approach to Reynolds number independence is

delayed for the case of mean vorticity, which is dictated more by the smaller scales of motion. For the small tank an approximate Reynolds number independent behavior can be observed above Re=45000 and for the large tank even a higher Reynolds number needs to be reached before attaining full Reynolds number independence. The difference between the two tanks decreases with increasing Reynolds number, however, a complete collapse is not observed.

Nondimensional dissipation associated with the phase-averaged mean flow can be defined as

$$e_{\mathrm{m}} = 2\frac{\partial\langle u_i\rangle}{\partial x_j}\frac{\partial\langle u_i\rangle}{\partial x_j}, \tag{5}$$

where all the nine components of the gradient of the mean velocity field can be obtained from the measurements on the three vertical plane. The resulting dissipation can then be interpolated onto the cylindrical surface at $r\approx1.06$. A contour plot of e_{m} for the small tank is shown in figures 14a and 14b for the two Reynolds numbers Re=4,330 and Re=63,180. The distribution is similar to that of vorticity and the primary contribution to dissipation from the mean flow appears to be associated the tip vortex pair. Again the distribution is qualitatively similar for both the Reynolds numbers, however, the magnitude of dissipation decreases with increasing Reynolds number. The corresponding dissipation fields for the large tank for Re=4,229 and Re=78,308 are shown in frames (c) and (d). As with the vorticity field, the dissipation of the mean flow is higher for the large tank.

It must be cautioned that, owing to the quadratic dependence of dissipation on velocity, e_{m} does not correspond to the mean dissipation one would obtain from an ensemble average of dissipation computed at individual instances. In the present set of experiments, since the individual realizations on the different vertical planes are temporally uncorrelated, it is not possible to compute the instantaneous dissipation accurately. e_{m} simply represents dissipation associated with the phase-averaged mean flow and its magnitude can be expected to be much smaller than mean dissipation, since the fluctuating small scales play the dominant role in dissipative process. The surface averaged dissipation as a function of Re for the two different tanks is shown in figure 15a and the corresponding trend of the surface maximum e_{m} is shown in figure 15b. The approach to Reynolds number independence is similar to that for mean vorticity observed in figure 13.

4. Conclusions

Experimental measurements of flow induced by a Rushton turbine in an unbaffled stirred tank have been performed over a wide range of operating speeds. Two different tank sizes were used with water as the working fluid to cover a Reynolds number range of 4,000 to 80,000. Phase-locked stereoscopic PIV measurements were made on three different vertical planes near the impeller to obtain all three components of the impeller-induced flow. Instantaneous realizations were averaged to obtain the phase-averaged velocity on a 60^0 sector of a cylindrical plane of nondimensional radial location, r»1.06, just beyond the blade tip radius. Data on this cylindrical surface dictates the flow in the interior of the tank. Hence, the Reynolds number scaling of this velocity data can serve as a proxy for the Reynolds number scaling of the entire flow. The phase-averaged velocity is dependent on both q and z, from which q-averaged and surface-averaged mean velocities are deduced.

All three components of the mean velocity are observed to scale with the blade tip velocity beyond a Reynolds number of about 15,000, in agreement with the findings of previous researchers. Similar behavior is observed for the scaling of the maximum impeller-induced velocity as well.

The phase-averaged mean flow was decomposed into circumferential, jet and tip-vortex elements and the parameters associated with the tip vortex pairs (their location, orientation, circulation and size) and the circular jet (jet momentum, width and virtual origin) were extracted from the experimental measurements. It is observed that the nondimensional jet and tip vortex strength appears to become Reynolds number independent only at large Reynolds numbers. The thickness of the jet appears to scale with the dimensions of the impeller above a modest Reynolds number of about 20,000; however the diameter of the tip vortex does not appear to scale similarly. The virtual origin of the circular jet, however, shows only a slow tendency towards Reynolds number independence. In the case of tip vortex pairs, the location of their centers on the plane of mean flow measurement (r≈1.06) remains independent of Re and the tip vortex orientation (with respect to the radial direction), quickly approaches an asymptotic value of about 60^0 with increasing Reynolds number.

The scaling of the mean flow from the small to the large tank has shown the most intriguing behavior. Effort was taken to maintain geometric and dynamic similarity between the small and the large tank. In both the tanks a no-slip condition has been enforced at the top with a lid, thus avoiding the influence of a free surface and the associated Froude number. The Rushton turbine was also geometrically scaled from the small to the large tank; however, small differences exist between the two. Probably most important, the length of the turbine blade in the large tank was 3.45% proportionately longer than the blade in the

small tank. This additional blade area probably enhances the pumping efficiency and accounts for the larger radial velocity observed in the large tank. Differences exist in blade and disk thickness as well. These differences were initially thought to be not significant, but because of them the Reynolds number behaviors for the two tanks, although similar, were not perfect. As a result noticeable difference persisted in the mean radial velocity between the small and the large tanks, even at asymptotically large Reynolds numbers (see figure 7). These results suggest a sensitive dependence of the mean flow to the overall geometric details of the impeller. Further conformation of this behavior requires additional experiments with perfectly scaled impellers, and perhaps over a series of tank sizes. The main conclusion to be drawn is that scale-up will not work well unless *all* aspects of the turbine blade are scaled perfectly.

The distribution of radial vorticity and dissipation illustrate the importance of the tip vortex contribution to the mean flow. The spatial compactness of the tip vortex pairs contributes to higher gradients and thus to gradient dependent quantities such as vorticity and dissipation. Reynolds number independence for the nondimensional vorticity and dissipation is observed above a Reynolds number of about 45,000 and the difference between the small and large tanks persist even at the higher Reynolds numbers.

Acknowledgments

This work was supported by a grant from National Science Foundation (CTS-9910543) and a gift from the Dow Chemical Company.

References

1. Desouza, A. and Pike, R.W. Fluid dynamics and flow patterns in stirred tanks with a turbine impeller, *Can. J. Chem. Engng.*, **50**, 15 (1972).
2. Van't Riet, K. and Smith, J.M. The trailing vortex system produced by Rushton turbine agitators, *Chem. Engng. Sci.*, **30**, 1093 (1975).
3. van der Molen, K. and van Maanen, H.R.E. Laser-Doppler measurements of the turbulent flow in stirred vessels to establish scaling rules, *Chem. Engng. Sci.*, **33**, 1161, (1978).
4. Kolar, V., Filip, P. and Curev, A.G. Hydrodynamics of a radially discharging impeller stream in agitated vessels, *Chem. Engng. Comm.*, **27**, 313 (1984).
5. Costes, J. and Couderc, J.P. Study by laser Doppler anemometry of the turbulent flow induced by a Rushton turbine in a stirred tank: influence of the size of the units I: mean flow and turbulence, *Chem Engng. Sci.*, **43**, 2765, (1988).
6. Costes, J. and Couderc, Chem Engng. Sci., Study by laser Doppler anemometry of the turbulent flow induced by a Rushton turbine in a stirred tank: influence of the size of the units I: mean flow and turbulence, *Chem Engng. Sci.*, **43**, 2765, (1988).
7. Dong, L., Johansen, S.T. and Engh, T.A. Flow induced by an impeller in an unbaffled tank – I. Experimental, *Chem Engng Sci.*, **49**, 549, (1994).
8. Sturesson, C., Theliander, H. and Rasmuson, A. An experimental (LDA) and numerical study of the turbulent flow behavior in the near wall and bottom regions in an axially stirred vessel, *AICHE Symp Series*, **91**, 102, (1995).
9. Stoots, C.M. and Calabrese, R.V. Mean velocity field relative to a Rushton turbine blade *AICHE J.*, **41**, pp 1, 1995.
10. Ducoste, J.J., Clark, M.M. and Weetman, R.J. Turbulence in flocculators: effect of tank size and impeller type, *AICHE J.*, **43**, 328, (1997).
11. Kemoun, A., Lusseyran, F., Mallet, J. and Mahousat, M. Experimental scanning for simplifying the model of a stirred-tank flow, *Exp. Fluids*, **25**, 23, (1998).
12. Lamberto, D.J., Alvarez, M.M. and Muzzio, F.J. Experimental and computational investigation of the laminar flow structure in a stirred tank, *Chem Engng. Sci.*, **54**, 919, (1999).
13. Montante, G., Lee, K.C., Brucato A. and Yianneskis, M. An experimental study of double-to-single-loop transition in stirred vessels, *Canadian J. Chem Engng.*, **77**, 649, (1999).

14. Yoon, H.S., Balachandar, S., Ha, M.Y. and Kar, K. Large eddy simulation of flow in a stirred tank, *J. Fluids Engng.*, **125**, 486 (2002).
15. Yoon, H.S., Sharp, K.V., Hill, D.F., Adrian, R.J., Balachandar, S., Ha, M.Y. and Kar, K. Integrated experimental and computational approach to simulation of flow in a stirred tank, *Chem. Engng. Sci.*, **56**, 6635, (2001).
16. Hill, D.F., Sharp, K.V. and Adrian, R.J. Stereoscopic particle image velocimetry measurements of the flow around a rushton turbine, *Exp. Fluids*, **29**, 478 (2000).
17. Kolar, V., Filip, P. and Curev, A.G. The swirling radial jet, *Apl. Sci. Res.*, **39**, 329-335 (1982).
18. Kresta, S.M. and Wood, P.E. Prediction of the three-dimensional turbulent flow in stirred tanks, *AIChE. J.*, **37**, 448-460 (1991).
19. Yianneskis, M., Popiolek, Z. and Whitelaw, J.H. An experimental study of the steady and unsteady flow characteristics of stirred reactors, *J. Fluid Mech.*, **175**, 537 (1987).

Figure Captions

Figure 1. Overhead schematic of experimental apparatus and data acquisition system.

Figure 2. Side and top view details of the tank and the impeller. Details of the three data acquisition planes and the cylindrical interpolation surface.

Figure 3. (a) The in-plane velocity vector plot and (b) the out-of-plane radial velocity contours of the phase-averaged mean flow at Re=4300 for the Small tank. (c) The in-plane velocity vector plot and (d) the out-of-plane radial velocity contours at Re=63180 for the Small tank.

Figure 4. (a) The in-plane velocity vector plot and (b) the out-of-plane radial velocity contours of the phase-averaged mean flow at Re=4299 for the Large tank. (c) The in-plane velocity vector plot and (d) the out-of-plane radial velocity contours at Re=62646 for the Large tank.

Figure 5. The normalized phase-averaged mean (a) radial, (b) circumferential and (c) axial velocities averaged over the circumferential direction ($\overline{\langle u_r \rangle}, \overline{\langle u_q \rangle}, \overline{\langle u_z \rangle}$); overbar indicated q -average) as a function of z for the different Reynolds numbers for the small tank.

Figure 6. The same as figure 5 for the large tank.

Figure 7. (a). The normalized phase-averaged mean radial, circumferential and axial velocities averaged over the entire $q-z$ plane ($\overline{\overline{\langle u_r \rangle}}, \overline{\overline{\langle u_q \rangle}}, \overline{\overline{\langle u_z \rangle}}$); the double overbar indicates a planar average) as a function of Reynolds numbers for the two different tank sizes. (b). The maximum (over the $q-z$ plane) phase-averaged mean radial, circumferential and axial velocities as a function of Reynolds number for the two different tanks.

Figure 8. (a). The scaling of jet momentum, A; (b) the inverse jet thickness, s ; and (c) the virtual origin, a , as a function of Reynolds number for the two different tanks.

Figure 9. The circumferential flow, u_c , as a function of axial location at $R \approx 1.06$ for the varying Reynolds numbers for (a) the small tank and (b) the large tank.

Figure 10. The experimental phase-averaged mean radial, circumferential and axial velocity components as a function of z for (a) the small tank at $q = 55^0$ and $\mathrm{Re} = 23700$ and (b) the large tank at $q = 50^0$ and $\mathrm{Re} = 23492$. Also shown for comparison are the corresponding velocities from the theoretical jet model.

Figure 11. (a) The scaling of vortex strength, G and (b) the vortex size, $1/\sqrt{d}$, as a function of Reynolds numbers for the two different tank sizes.

Figure 12. (a) The in-plane velocity vector plot and (b) the out-of-plane radial velocity contours obtained from the experiments in the large tank at Re=23492, after subtraction of the theoretical jet and circumferential flow, so that attention can be focused on only the tip vortex.

Figure 13. Same as figure 12 obtained using the tip vortex model.

Figure 14. Contours of mean radial vorticity plotted on the *q*-*z* plane at $R \approx 1.06$ for the small tank at (a) Re=4300, (b) Re=63180 and for the large tank at (c) Re=4229 and (d) Re=78308.

Figure 15. (a) The square-root of surface-averaged mean square vorticity, $\sqrt{\overline{\overline{\langle w_r \rangle}}}$, plotted as a function of Re for the two different tanks, (b) the corresponding trend of the surface maximum radial vorticity.

Figure 16. Contours of dissipation associated with the mean velocity plotted on the *q*-*z* plane at $R \approx 1.06$ for the small tank at (a) Re=4300, (b) Re=63180 and for the large tank at (c) Re=4229 and (d) Re=78308.

Figure 17. (a) The surface-averaged dissipation of mean flow plotted as a function of Re for the two different tanks, (b) the corresponding trend of the surface maximum.

Small Tank		Large Tank	
Ω (rpm)	Re=ND^2/n	Ω (rpm)	Re=ND^2/n
100	4293	27	4229
150	6440	41	6421
367	15756	100	15662
551	23655	150	23492
734	31512	200	31323
1102	47311	300	46985
1469	63066	400	62646
		500	78308

Table 1. Rotational speed and Reynolds numbers of experimental data sets.

Re $=ND^2/n$	$\pm z_v$	q_v	f_v
4300	**0.08**	**18^0**	**56.3^0**
6450	**0.08**	**19^0**	**56.43^0**
15785	**0.085**	**19^0**	**52.23^0**
23700	**0.085**	**24^0**	**55.6^0**
31570	**0.087**	**21^0**	**57.87^0**
47400	**0.087**	**21^0**	**58.63^0**
63180	**0.087**	**21^0**	**59.35^0**

Re $=ND^2/n$	$\pm z_v$	q_v	f_v
4229	**0.087**	**12^0**	**48.41^0**
6421	**0.091**	**12^0**	**51.94^0**
15662	**0.092**	**15^0**	**57.1^0**
23492	**0.093**	**16^0**	**57.15^0**
31323	**0.094**	**16^0**	**57.5^0**
46985	**0.09**	**15^0**	**59.27^0**

	6		
62646	**0.09**	**13^0**	**58.4^0**
78308	**0.09**	**16^0**	**59.61^0**

Table 2. The vortex parameters: $\pm z_v$, the axial location of vortex center from the midplane, q_v, the angle between the vortex center and the nearest blade, f_v, the angle between the vortex backbone and the local radial direction at the point where it intersect the cylindrical plane.

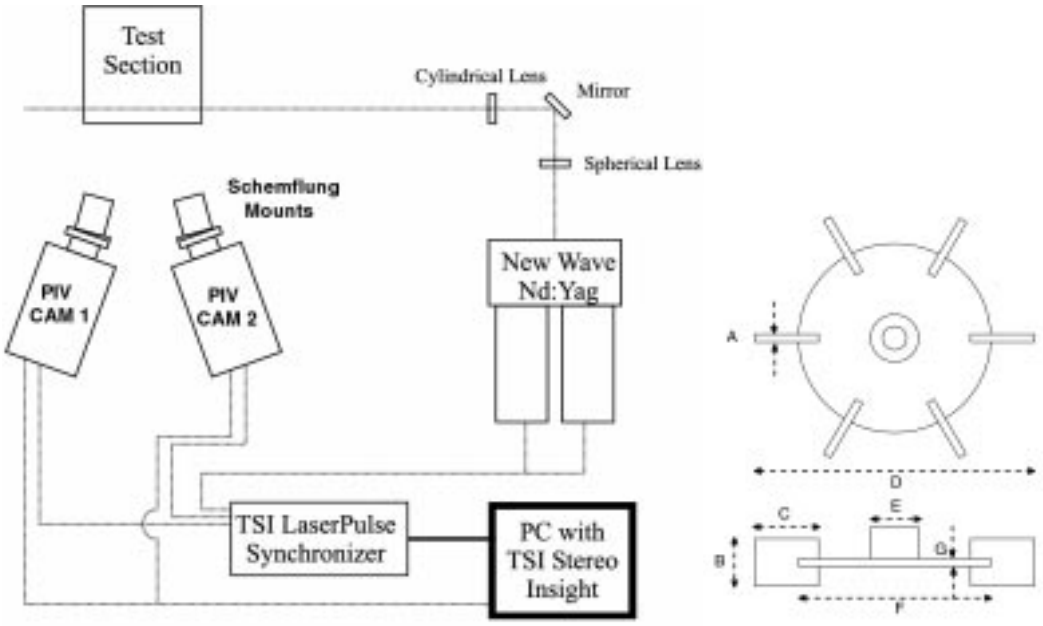

	Small Tank (in mm)	Large Tank (in mm)	Ratio
T	152.5	292.1	1.92
A	2.19	3.53	1.61
B	10.28	19.54	1.9
C	12.37	24.50	1.98
D	50.59	97.20	1.92
E	12.51	15.98	1.28
F	33.16	63.20	1.91
G	2.40	3.44	1.43

Figure 1. Overhead schematic of experimental apparatus and data acquisition system.

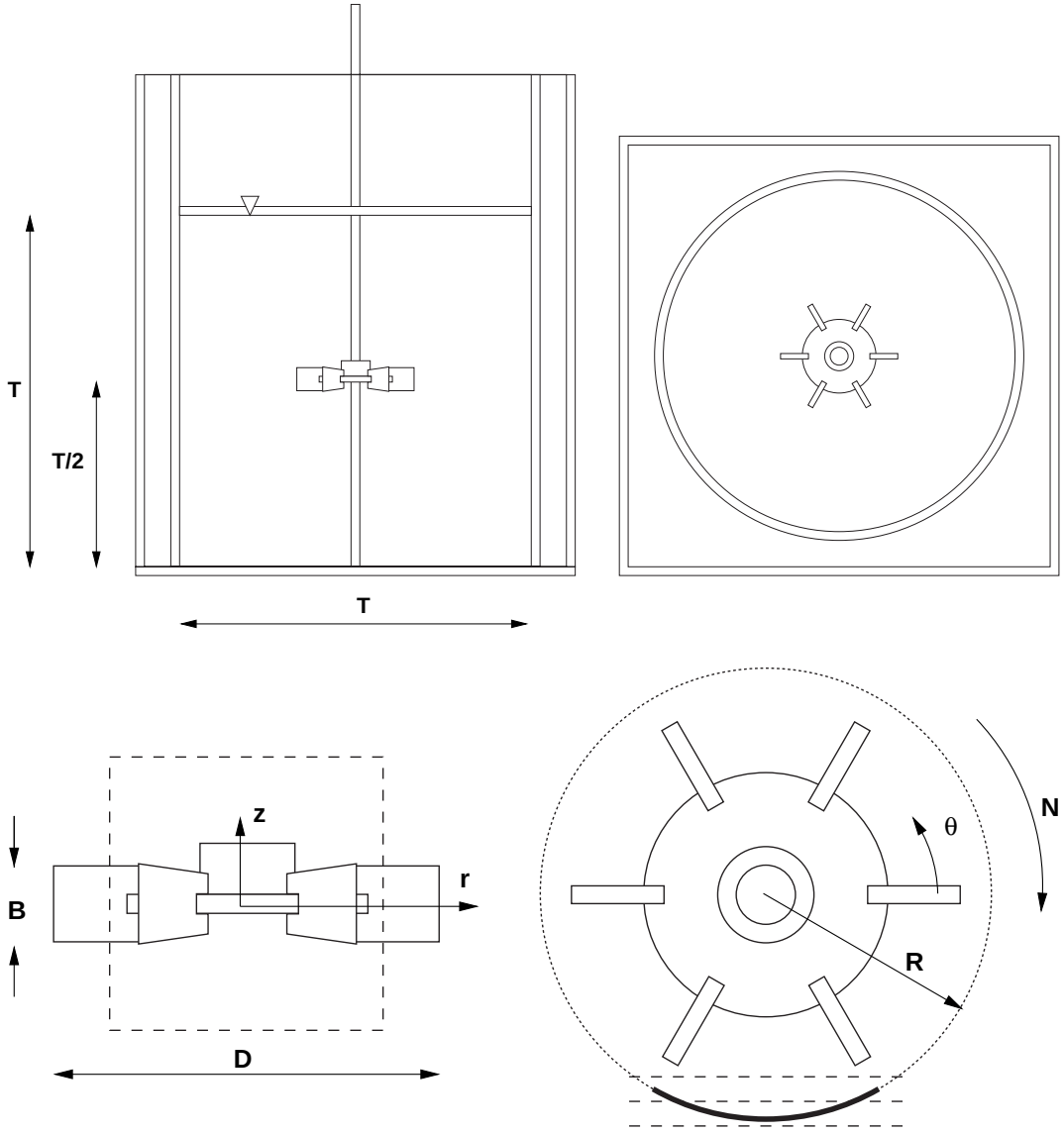

Figure 2. Side and top view details of the tank and the impeller. Details of the three data acquisition planes and the cylindrical interpolation surface of radius, R, are shown.

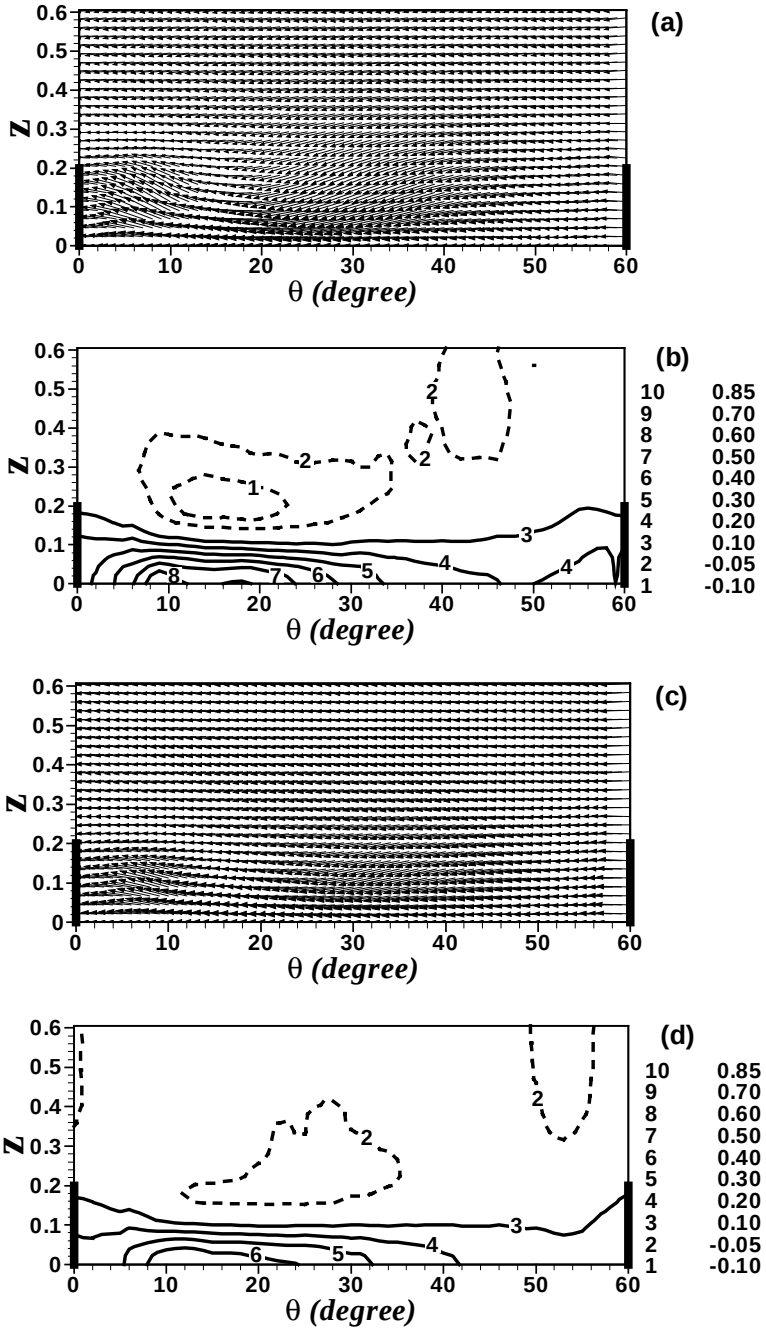

Figure 3. (a) The in-plane velocity vector plot and (b) the out-of-plane radial velocity contours of the phase-averaged mean flow at Re=4,300 for the small tank. (c) The in-plane velocity vector plot and (d) the out-of-plane radial velocity contours at Re=63,180 for the small tank.

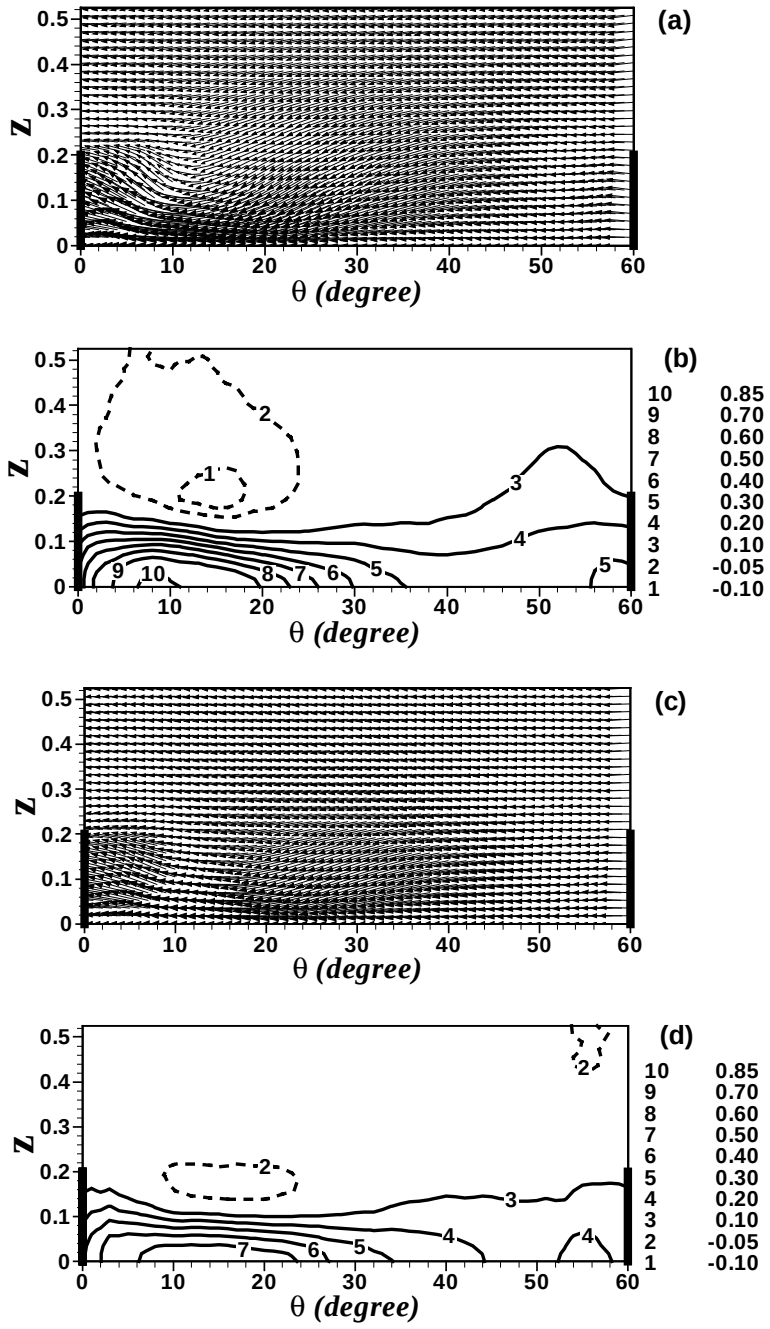

Figure 4. (a) The in-plane velocity vector plot and (b) the out-of-plane radial velocity contours of the phase-averaged mean flow at Re=4,299 for the large tank. (c) The in-plane velocity vector plot and (d) the out-of-plane radial velocity contours at Re=62,646 for the large tank.

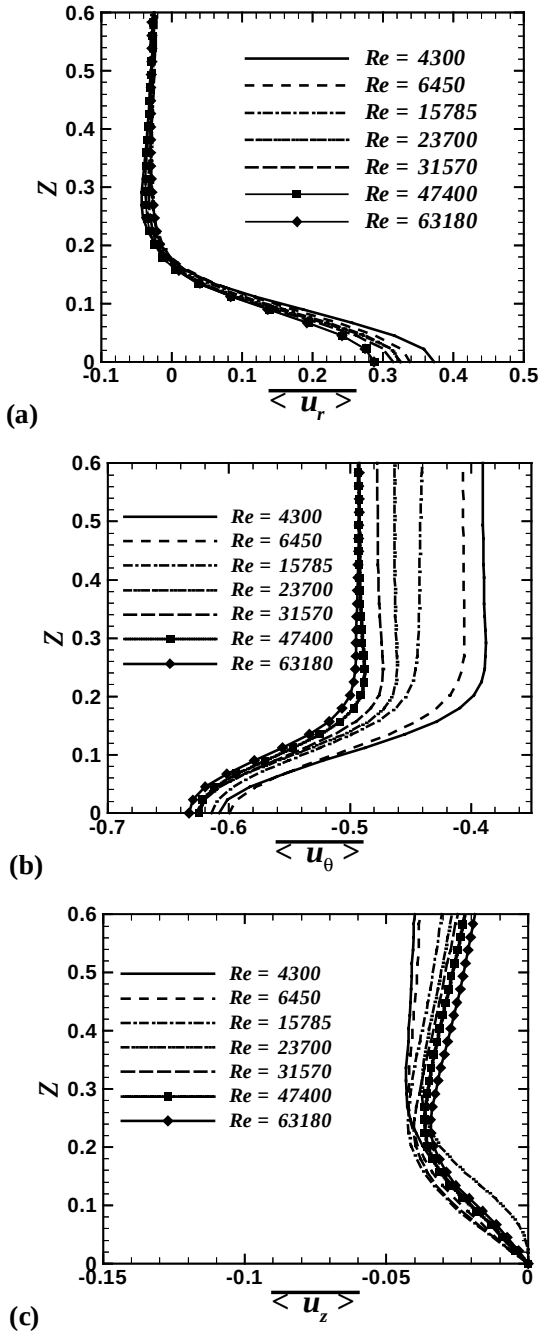

Figure 5. The normalized phase-averaged mean (a) radial, (b) circumferential and (c) axial velocities averaged over the circumferential direction, $\overline{\langle u_r \rangle}, \overline{\langle u_\theta \rangle}, \overline{\langle u_z \rangle}$ (overbar indicates θ-average) for the small tank.

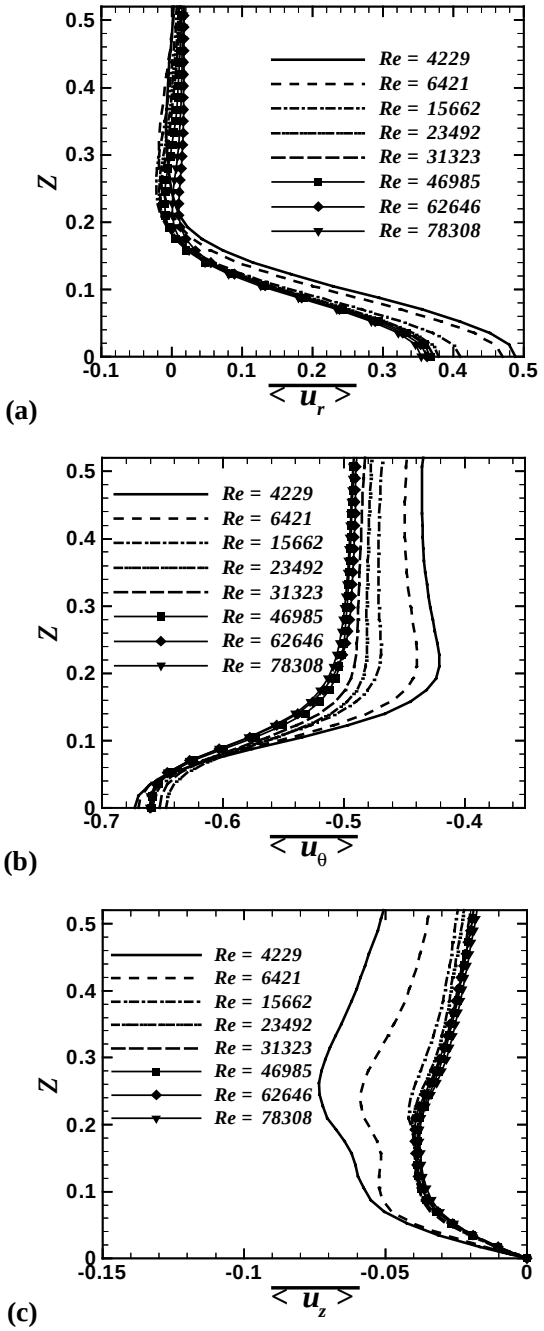

Figure 6. The same as figure 5 for the large tank.

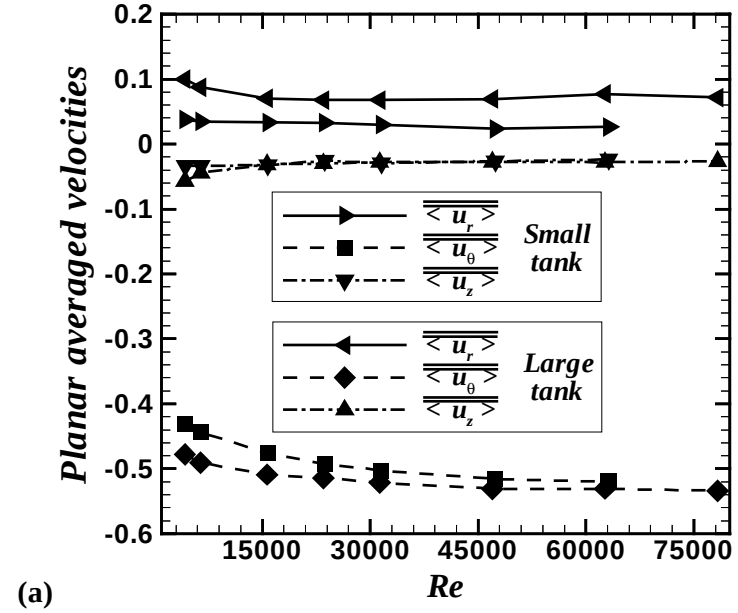

Figure 7. (a). The normalized phase-averaged mean radial, circumferential and axial velocities averaged over the entire $\theta - z$ plane ($\overline{\overline{\langle u_r \rangle}}, \overline{\overline{\langle u_\theta \rangle}}, \overline{\overline{\langle u_z \rangle}}$); the double overbar indicates a planar average) as a function of Reynolds numbers for the two different tank sizes. (b). The maximum (over the $\theta - z$ plane) phase-averaged mean radial, circumferential and axial velocities as a function of Reynolds number for the two different tanks.

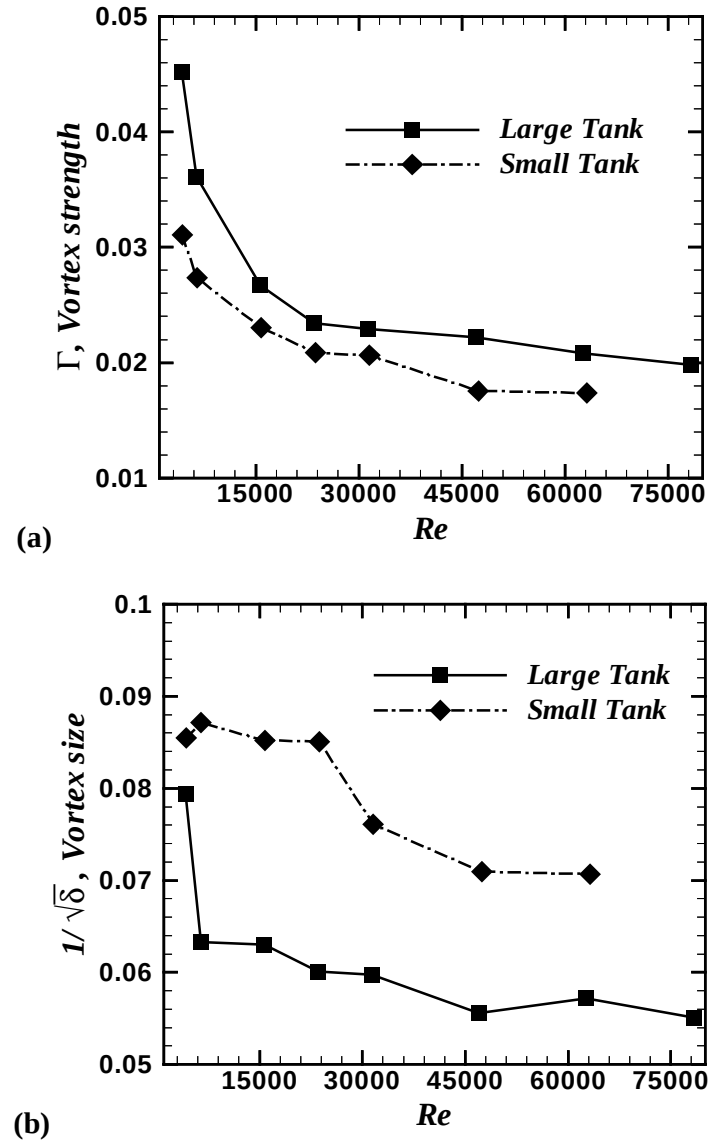

Figure 8. (a) The scaling of nondimensional vortex strength, Γ and (b) the nondimensional vortex size, $1/\sqrt{\delta}$, as a function of Reynolds numbers for the two different tank sizes.

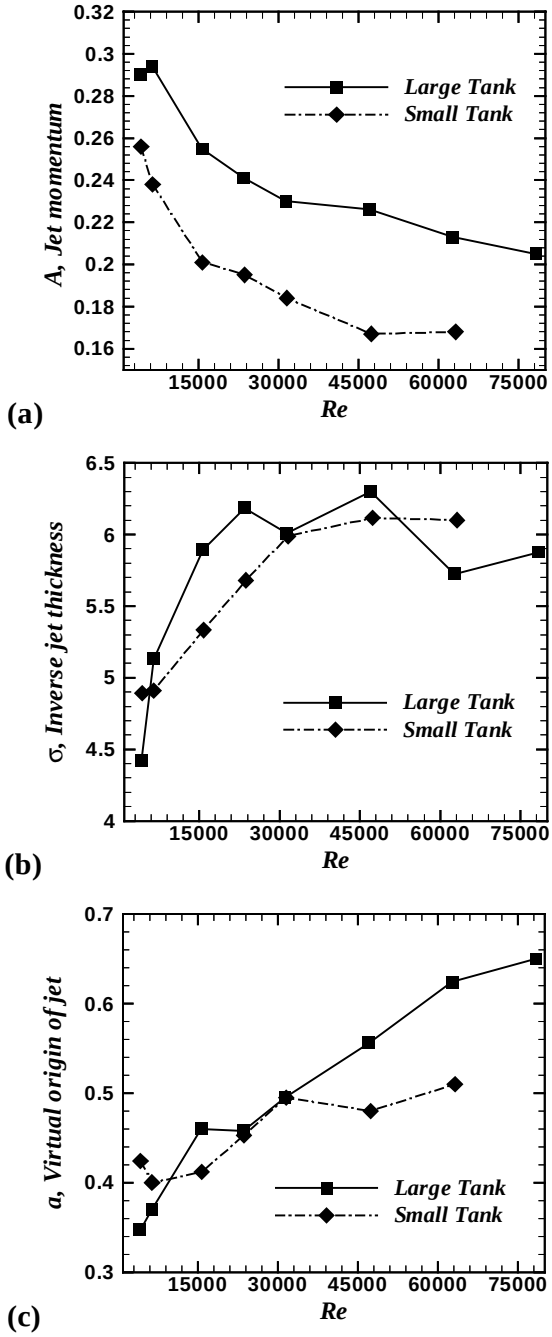

Figure 9. (a). The scaling of the nondimensional jet momentum, A; (b) the inverse jet thickness, σ; and (c) the virtual origin, a, as a function of Reynolds number for the two different tanks.

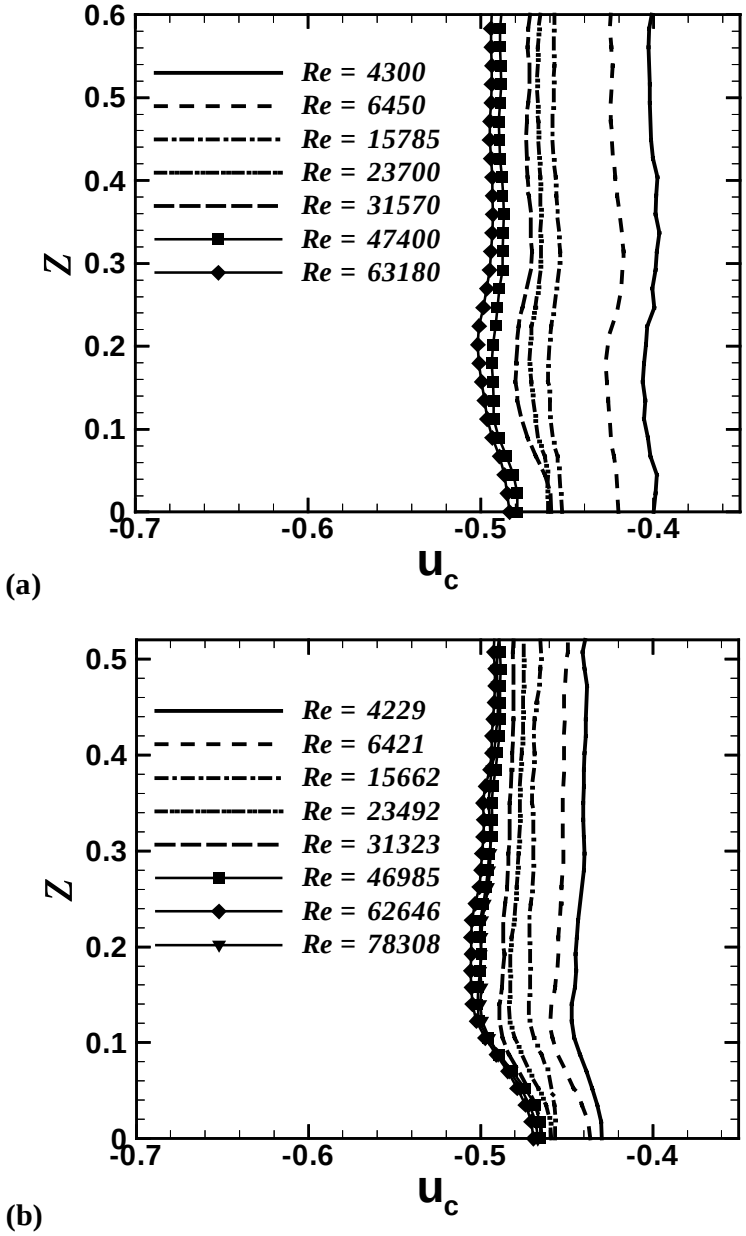

Figure 10. The circumferential flow element, u_c, as a function of axial location at $r \approx 1.06$ for the varying Reynolds numbers for (a) the small tank and (b) the large tank.

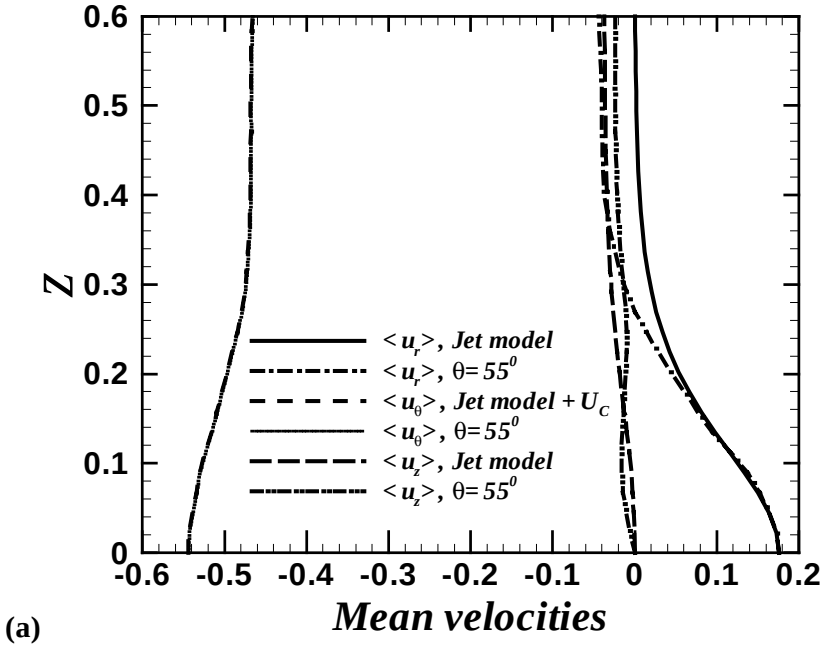

(a)

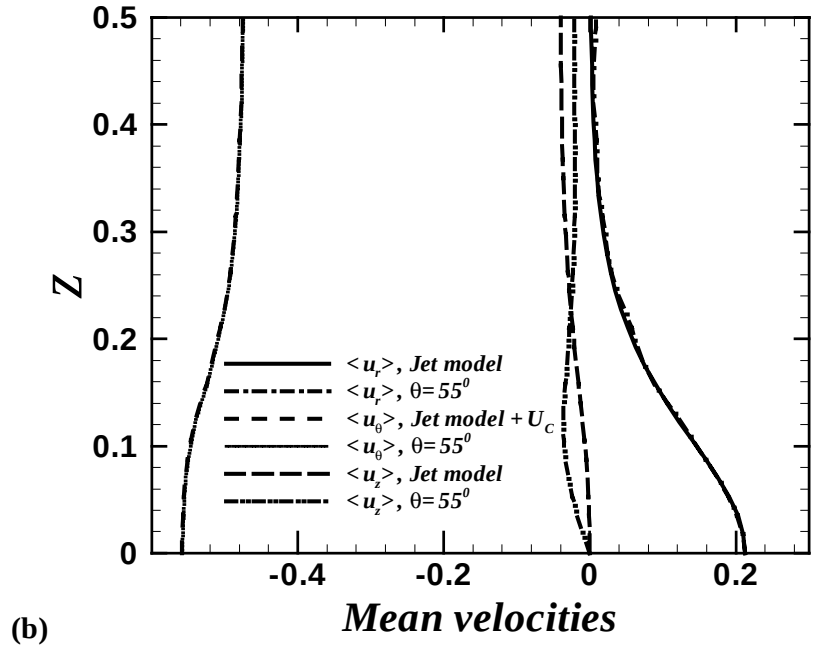

(b)

Figure 11. The experimental phase-averaged mean radial, circumferential and axial velocity components as a function of z for (a) the small tank at $\theta = 55^0$ and $\mathrm{Re} = 23,700$ and (b) the large tank at $\theta = 50^0$ and $\mathrm{Re} = 23,492$. Also shown for comparison are the corresponding velocities from the theoretical jet model.

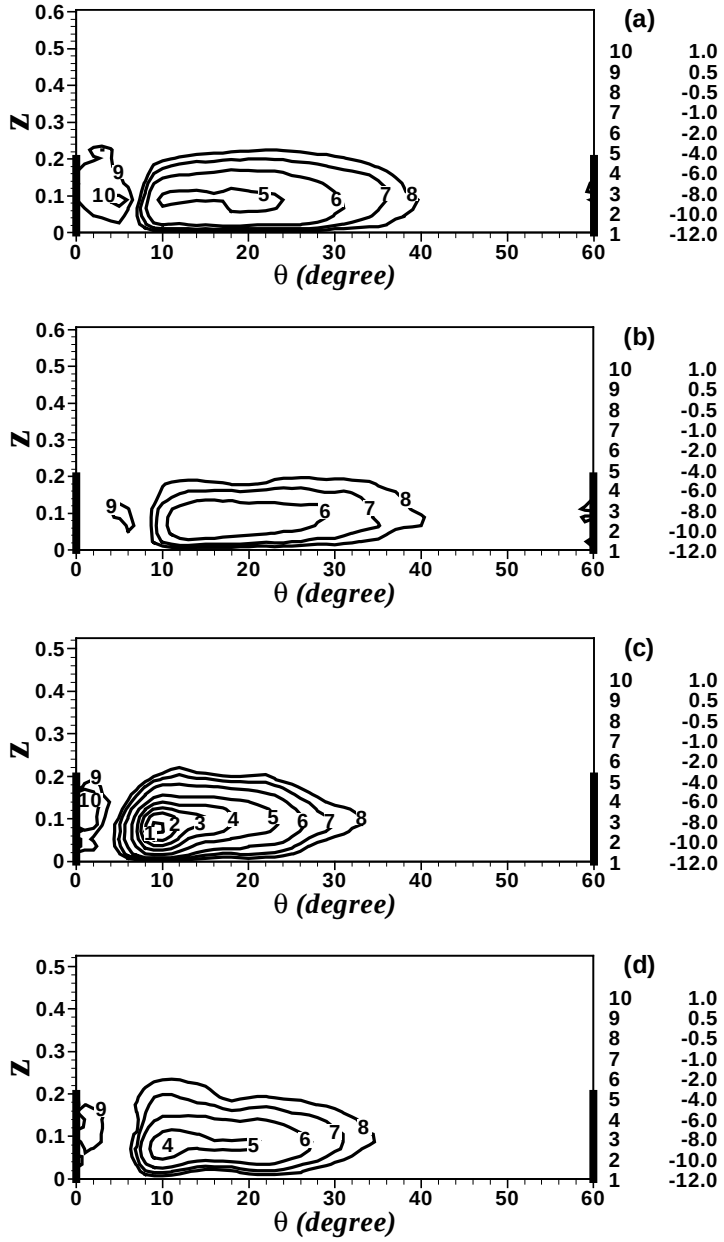

Figure 12. Contours of mean radial vorticity plotted on the θ-z plane at $r \approx 1.06$ for the small tank at (a) Re=4,300, (b) Re=63,180 and for the large tank at (c) Re=4,229 and (d) Re=78,308.

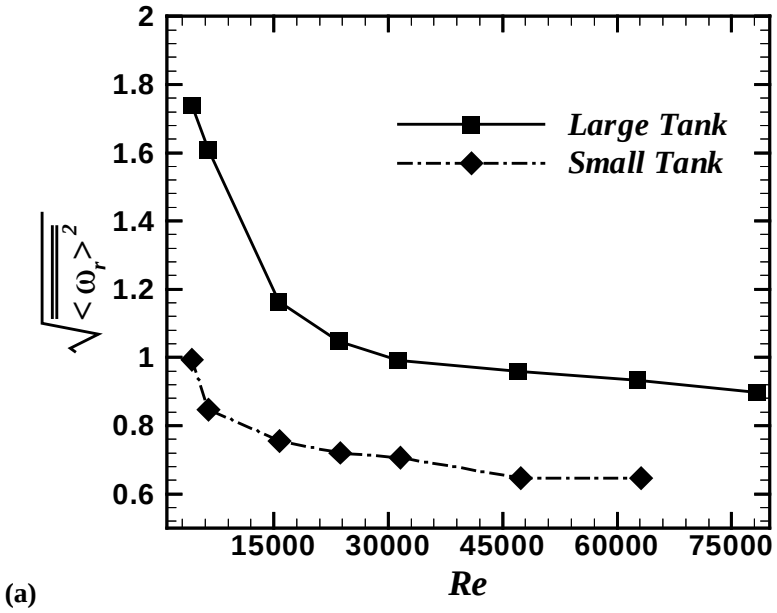

(a)

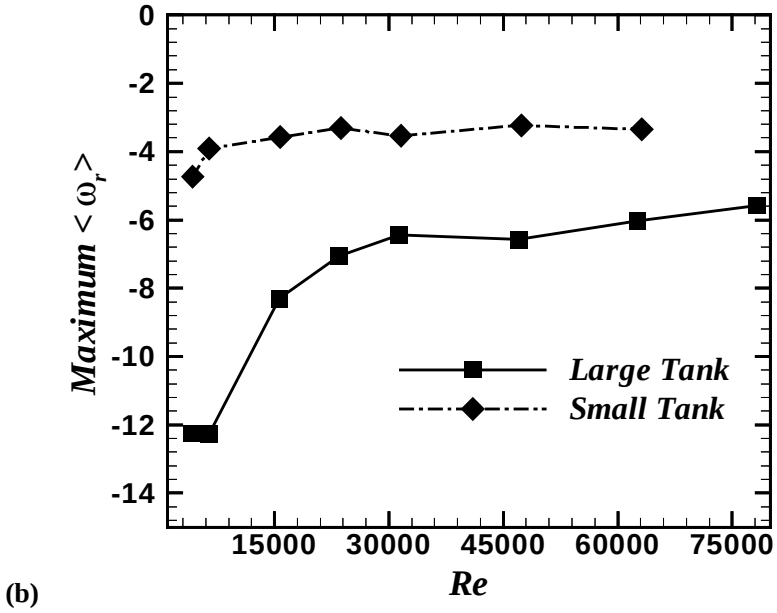

(b)

Figure 13. (a) The square-root of surface-averaged mean square vorticity, $\sqrt{\langle \omega_r \rangle}$, plotted as a function of Re for the two different tanks, (b) the corresponding trend of the surface maximum radial vorticity.

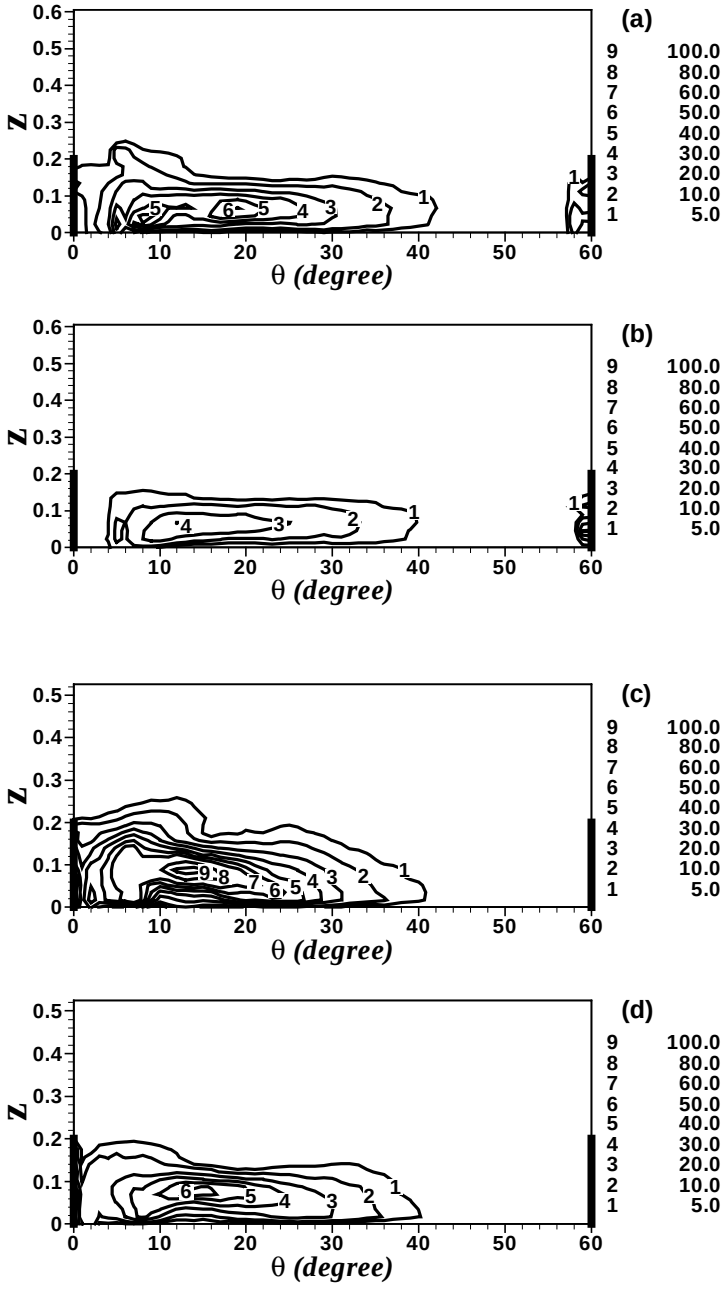

Figure 14. Contours of dissipation associated with the mean velocity plotted on the θ-z plane at $r \approx 1.06$ for the small tank at (a) Re=4,300, (b) Re=63,180 and for the large tank at (c) Re=4,229 and (d) Re=78,308.

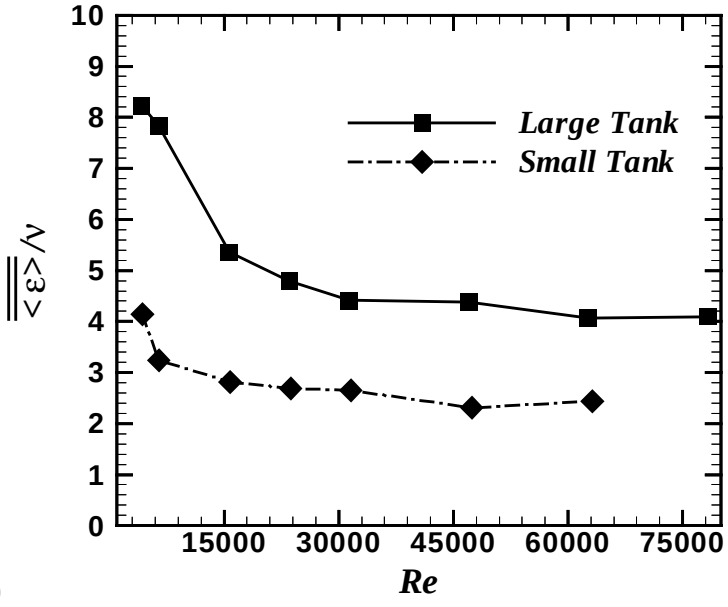

(a)

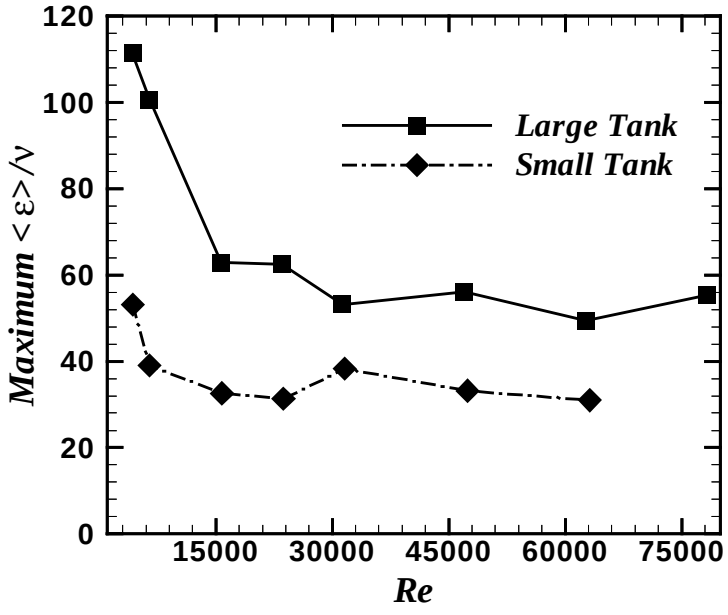

(b)

Figure 15. (a) The surface-averaged dissipation of mean flow plotted as a function of Re for the two different tanks, (b) the corresponding trend of the surface maximum.

List of Recent TAM Reports

No.	Authors	Title	Date
947	Kessler, M. R., and S. R. White	Self-activated healing of delamination damage in woven composites—*Composites A: Applied Science and Manufacturing* **32**, 683–699 (2001)	June 2000
948	Phillips, W. R. C.	On the pseudomomentum and generalized Stokes drift in a spectrum of rotational waves—*Journal of Fluid Mechanics* **430**, 209–229 (2001)	July 2000
949	Hsui, A. T., and D. N. Riahi	Does the Earth's nonuniform gravitational field affect its mantle convection?—*Physics of the Earth and Planetary Interiors* (submitted)	July 2000
950	Phillips, J. W.	Abstract Book, 20th International Congress of Theoretical and Applied Mechanics (27 August – 2 September, 2000, Chicago)	July 2000
951	Vainchtein, D. L., and H. Aref	Morphological transition in compressible foam—*Physics of Fluids* **13**, 2152–2160 (2001)	July 2000
952	Chaïeb, S., E. Sato-Matsuo, and T. Tanaka	Shrinking-induced instabilities in gels	July 2000
953	Riahi, D. N., and A. T. Hsui	A theoretical investigation of high Rayleigh number convection in a nonuniform gravitational field—*International Journal of Pure and Applied Mathematics*, in press (2003)	Aug. 2000
954	Riahi, D. N.	Effects of centrifugal and Coriolis forces on a hydromagnetic chimney convection in a mushy layer—*Journal of Crystal Growth* **226**, 393–405 (2001)	Aug. 2000
955	Fried, E.	An elementary molecular-statistical basis for the Mooney and Rivlin–Saunders theories of rubber-elasticity—*Journal of the Mechanics and Physics of Solids* **50**, 571–582 (2002)	Sept. 2000
956	Phillips, W. R. C.	On an instability to Langmuir circulations and the role of Prandtl and Richardson numbers—*Journal of Fluid Mechanics* **442**, 335–358 (2001)	Sept. 2000
957	Chaïeb, S., and J. Sutin	Growth of myelin figures made of water soluble surfactant—Proceedings of the 1st Annual International IEEE–EMBS Conference on Microtechnologies in Medicine and Biology (October 2000, Lyon, France), 345–348	Oct. 2000
958	Christensen, K. T., and R. J. Adrian	Statistical evidence of hairpin vortex packets in wall turbulence—*Journal of Fluid Mechanics* **431**, 433–443 (2001)	Oct. 2000
959	Kuznetsov, I. R., and D. S. Stewart	Modeling the thermal expansion boundary layer during the combustion of energetic materials—*Combustion and Flame*, in press (2001)	Oct. 2000
960	Zhang, S., K. J. Hsia, and A. J. Pearlstein	Potential flow model of cavitation-induced interfacial fracture in a confined ductile layer—*Journal of the Mechanics and Physics of Solids*, **50**, 549–569 (2002)	Nov. 2000
961	Sharp, K. V., R. J. Adrian, J. G. Santiago, and J. I. Molho	Liquid flows in microchannels—Chapter 6 of *CRC Handbook of MEMS* (M. Gad-el-Hak, ed.) (2001)	Nov. 2000
962	Harris, J. G.	Rayleigh wave propagation in curved waveguides—*Wave Motion* **36**, 425–441 (2002)	Jan. 2001
963	Dong, F., A. T. Hsui, and D. N. Riahi	A stability analysis and some numerical computations for thermal convection with a variable buoyancy factor—*Journal of Theoretical and Applied Mechanics* **2**, 19–46 (2002)	Jan. 2001
964	Phillips, W. R. C.	Langmuir circulations beneath growing or decaying surface waves—*Journal of Fluid Mechanics* (submitted)	Jan. 2001
965	Bdzil, J. B., D. S. Stewart, and T. L. Jackson	Program burn algorithms based on detonation shock dynamics—*Journal of Computational Physics* (submitted)	Jan. 2001
966	Bagchi, P., and S. Balachandar	Linearly varying ambient flow past a sphere at finite Reynolds number: Part 2—Equation of motion—*Journal of Fluid Mechanics* **481**, 105–148 (2003) (with change in title)	Feb. 2001

List of Recent TAM Reports (cont'd)

No.	*Authors*	*Title*	*Date*
967	Cermelli, P., and E. Fried	The evolution equation for a disclination in a nematic fluid—*Proceedings of the Royal Society A* **458**, 1–20 (2002)	Apr. 2001
968	Riahi, D. N.	Effects of rotation on convection in a porous layer during alloy solidification—Chapter 12 in *Transport Phenomena in Porous Media* (D. B. Ingham and I. Pop, eds.), 316–340 (2002)	Apr. 2001
969	Damljanovic, V., and R. L. Weaver	Elastic waves in cylindrical waveguides of arbitrary cross section—*Journal of Sound and Vibration* (submitted)	May 2001
970	Gioia, G., and A. M. Cuitiño	Two-phase densification of cohesive granular aggregates—*Physical Review Letters* **88**, 204302 (2002) (in extended form and with added co-authors S. Zheng and T. Uribe)	May 2001
971	Subramanian, S. J., and P. Sofronis	Calculation of a constitutive potential for isostatic powder compaction—*International Journal of Mechanical Sciences* (submitted)	June 2001
972	Sofronis, P., and I. M. Robertson	Atomistic scale experimental observations and micromechanical/continuum models for the effect of hydrogen on the mechanical behavior of metals—*Philosophical Magazine* (submitted)	June 2001
973	Pushkin, D. O., and H. Aref	Self-similarity theory of stationary coagulation—*Physics of Fluids* **14**, 694–703 (2002)	July 2001
974	Lian, L., and N. R. Sottos	Stress effects in ferroelectric thin films—*Journal of the Mechanics and Physics of Solids* (submitted)	Aug. 2001
975	Fried, E., and R. E. Todres	Prediction of disclinations in nematic elastomers—*Proceedings of the National Academy of Sciences* **98**, 14773–14777 (2001)	Aug. 2001
976	Fried, E., and V. A. Korchagin	Striping of nematic elastomers—*International Journal of Solids and Structures* **39**, 3451–3467 (2002)	Aug. 2001
977	Riahi, D. N.	On nonlinear convection in mushy layers: Part I. Oscillatory modes of convection—*Journal of Fluid Mechanics* **467**, 331–359 (2002)	Sept. 2001
978	Sofronis, P., I. M. Robertson, Y. Liang, D. F. Teter, and N. Aravas	Recent advances in the study of hydrogen embrittlement at the University of Illinois—Invited paper, Hydrogen–Corrosion Deformation Interactions (Sept. 16–21, 2001, Jackson Lake Lodge, Wyo.)	Sept. 2001
979	Fried, E., M. E. Gurtin, and K. Hutter	A void-based description of compaction and segregation in flowing granular materials—*Proceedings of the Royal Society of London A* (submitted)	Sept. 2001
980	Adrian, R. J., S. Balachandar, and Z.-C. Liu	Spanwise growth of vortex structure in wall turbulence—*Korean Society of Mechanical Engineers International Journal* **15**, 1741–1749 (2001)	Sept. 2001
981	Adrian, R. J.	Information and the study of turbulence and complex flow—*Japanese Society of Mechanical Engineers Journal B*, in press (2002)	Oct. 2001
982	Adrian, R. J., and Z.-C. Liu	Observation of vortex packets in direct numerical simulation of fully turbulent channel flow—*Journal of Visualization*, in press (2002)	Oct. 2001
983	Fried, E., and R. E. Todres	Disclinated states in nematic elastomers—*Journal of the Mechanics and Physics of Solids* **50**, 2691–2716 (2002)	Oct. 2001
984	Stewart, D. S.	Towards the miniaturization of explosive technology—Proceedings of the 23rd International Conference on Shock Waves (2001)	Oct. 2001
985	Kasimov, A. R., and Stewart, D. S.	Spinning instability of gaseous detonations—*Journal of Fluid Mechanics* (submitted)	Oct. 2001
986	Brown, E. N., N. R. Sottos, and S. R. White	Fracture testing of a self-healing polymer composite—*Experimental Mechanics* (submitted)	Nov. 2001
987	Phillips, W. R. C.	Langmuir circulations—*Surface Waves* (J. C. R. Hunt and S. Sajjadi, eds.), in press (2002)	Nov. 2001
988	Gioia, G., and F. A. Bombardelli	Scaling and similarity in rough channel flows—*Physical Review Letters* **88**, 014501 (2002)	Nov. 2001
989	Riahi, D. N.	On stationary and oscillatory modes of flow instabilities in a rotating porous layer during alloy solidification—*Journal of Porous Media*, in press (2002)	Nov. 2001

List of Recent TAM Reports (cont'd)

No.	Authors	Title	Date
990	Okhuysen, B. S., and D. N. Riahi	Effect of Coriolis force on instabilities of liquid and mushy regions during alloy solidification—*Physics of Fluids* (submitted)	Dec. 2001
991	Christensen, K. T., and R. J. Adrian	Measurement of instantaneous Eulerian acceleration fields by particle-image accelerometry: Method and accuracy—*Experimental Fluids* (submitted)	Dec. 2001
992	Liu, M., and K. J. Hsia	Interfacial cracks between piezoelectric and elastic materials under in-plane electric loading—*Journal of the Mechanics and Physics of Solids* **51**, 921–944 (2003)	Dec. 2001
993	Panat, R. P., S. Zhang, and K. J. Hsia	Bond coat surface rumpling in thermal barrier coatings—*Acta Materialia* **51**, 239–249 (2003)	Jan. 2002
994	Aref, H.	A transformation of the point vortex equations—*Physics of Fluids* **14**, 2395–2401 (2002)	Jan. 2002
995	Saif, M. T. A, S. Zhang, A. Haque, and K. J. Hsia	Effect of native Al_2O_3 on the elastic response of nanoscale aluminum films—*Acta Materialia* **50**, 2779–2786 (2002)	Jan. 2002
996	Fried, E., and M. E. Gurtin	A nonequilibrium theory of epitaxial growth that accounts for surface stress and surface diffusion—*Journal of the Mechanics and Physics of Solids* **51**, 487–517 (2003)	Jan. 2002
997	Aref, H.	The development of chaotic advection—*Physics of Fluids* **14**, 1315–1325 (2002); see also *Virtual Journal of Nanoscale Science and Technology*, 11 March 2002	Jan. 2002
998	Christensen, K. T., and R. J. Adrian	The velocity and acceleration signatures of small-scale vortices in turbulent channel flow—*Journal of Turbulence*, in press (2002)	Jan. 2002
999	Riahi, D. N.	Flow instabilities in a horizontal dendrite layer rotating about an inclined axis—*Proceedings of the Royal Society of London A*, in press (2003)	Feb. 2002
1000	Kessler, M. R., and S. R. White	Cure kinetics of ring-opening metathesis polymerization of dicyclopentadiene—*Journal of Polymer Science A* **40**, 2373–2383 (2002)	Feb. 2002
1001	Dolbow, J. E., E. Fried, and A. Q. Shen	Point defects in nematic gels: The case for hedgehogs—*Proceedings of the National Academy of Sciences* (submitted)	Feb. 2002
1002	Riahi, D. N.	Nonlinear steady convection in rotating mushy layers—*Journal of Fluid Mechanics* **485**, 279–306 (2003)	Mar. 2002
1003	Carlson, D. E., E. Fried, and S. Sellers	The totality of soft-states in a neo-classical nematic elastomer—*Proceedings of the Royal Society A* (submitted)	Mar. 2002
1004	Fried, E., and R. E. Todres	Normal-stress differences and the detection of disclinations in nematic elastomers—*Journal of Polymer Science B: Polymer Physics* **40**, 2098–2106 (2002)	June 2002
1005	Fried, E., and B. C. Roy	Gravity-induced segregation of cohesionless granular mixtures—*Lecture Notes in Mechanics*, in press (2002)	July 2002
1006	Tomkins, C. D., and R. J. Adrian	Spanwise structure and scale growth in turbulent boundary layers—*Journal of Fluid Mechanics* (submitted)	Aug. 2002
1007	Riahi, D. N.	On nonlinear convection in mushy layers: Part 2. Mixed oscillatory and stationary modes of convection—*Journal of Fluid Mechanics* (submitted)	Sept. 2002
1008	Aref, H., P. K. Newton, M. A. Stremler, T. Tokieda, and D. L. Vainchtein	Vortex crystals—*Advances in Applied Mathematics* **39**, in press (2002)	Oct. 2002
1009	Bagchi, P., and S. Balachandar	Effect of turbulence on the drag and lift of a particle—*Physics of Fluids*, in press (2003)	Oct. 2002
1010	Zhang, S., R. Panat, and K. J. Hsia	Influence of surface morphology on the adhesive strength of aluminum/epoxy interfaces—*Journal of Adhesion Science and Technology* (submitted)	Oct. 2002
1011	Carlson, D. E., E. Fried, and D. A. Tortorelli	On internal constraints in continuum mechanics—*Journal of Elasticity*, in press (2003)	Oct. 2002

List of Recent TAM Reports (cont'd)

No.	*Authors*	*Title*	*Date*
1012	Boyland, P. L., M. A. Stremler, and H. Aref	Topological fluid mechanics of point vortex motions—*Physica D* **175**, 69–95 (2002)	Oct. 2002
1013	Bhattacharjee, P., and D. N. Riahi	Computational studies of the effect of rotation on convection during protein crystallization—*Journal of Crystal Growth* (submitted)	Feb. 2003
1014	Brown, E. N., M. R. Kessler, N. R. Sottos, and S. R. White	*In situ* poly(urea-formaldehyde) microencapsulation of dicyclopentadiene—*Journal of Microencapsulation* (submitted)	Feb. 2003
1015	Brown, E. N., S. R. White, and N. R. Sottos	Microcapsule induced toughening in a self-healing polymer composite—*Journal of Materials Science* (submitted)	Feb. 2003
1016	Kuznetsov, I. R., and D. S. Stewart	Burning rate of energetic materials with thermal expansion—*Combustion and Flame* (submitted)	Mar. 2003
1017	Dolbow, J., E. Fried, and H. Ji	Chemically induced swelling of hydrogels—*Journal of the Mechanics and Physics of Solids*, in press (2003)	Mar. 2003
1018	Costello, G. A.	Mechanics of wire rope—Mordica Lecture, Interwire 2003, Wire Association International, Atlanta, Georgia, May 12, 2003	Mar. 2003
1019	Wang, J., N. R. Sottos, and R. L. Weaver	Thin film adhesion measurement by laser induced stress waves—*Journal of the Mechanics and Physics of Solids* (submitted)	Apr. 2003
1020	Bhattacharjee, P., and D. N. Riahi	Effect of rotation on surface tension driven flow during protein crystallization—*Microgravity Science and Technology* (submitted)	Apr. 2003
1021	Fried, E.	The configurational and standard force balances are not always statements of a single law—*Proceedings of the Royal Society* (submitted)	Apr. 2003
1022	Panat, R. P., and K. J. Hsia	Experimental investigation of the bond coat rumpling instability under isothermal and cyclic thermal histories in thermal barrier systems—*Proceedings of the Royal Society of London A* (submitted)	May 2003
1023	Fried, E., and M. E. Gurtin	A unified treatment of evolving interfaces accounting for small deformations and atomic transport: grain-boundaries, phase transitions, epitaxy—*Advances in Applied Mechanics*, in press (2003)	May 2003
1024	Dong, F., D. N. Riahi, and A. T. Hsui	On similarity waves in compacting media—*Advances in Mathematics Research* (submitted)	May 2003
1025	Liu, M., and K. J. Hsia	Locking of electric field induced non-180° domain switching and phase transition in ferroelectric materials upon cyclic electric fatigue—*Applied Physics Letters* (submitted)	May 2003
1026	Liu, M., K. J. Hsia, and M. Sardela Jr.	In situ X-ray diffraction study of electric field induced domain switching and phase transition in PZT-5H—*Journal of the American Ceramics Society* (submitted)	May 2003
1027	Riahi, D. N.	On flow of binary alloys during crystal growth—*Recent Research Development in Crystal Growth*, in press (2003)	May 2003
1028	Riahi, D. N.	On fluid dynamics during crystallization—*Recent Research Development in Fluid Dynamics* (submitted)	July 2003
1029	Fried, E., V. Korchagin, and R. E. Todres	Biaxial disclinated states in nematic elastomers—*Journal of Chemical Physics* (submitted)	July 2003
1030	Sharp, K. V., and R. J. Adrian	Transition from laminar to turbulent flow in liquid filled microtubes—*Physics of Fluids* (submitted)	July 2003
1031	Yoon, H. S., D. F. Hill, S. Balachandar, R. J. Adrian, and M. Y. Ha	Reynolds number scaling of flow in a Rushton turbine stirred tank: Part I—Mean flow, circular jet and tip vortex scaling—*Chemical Engineering Science* (submitted)	Aug. 2003
1032	Raju, R., S. Balachandar, D. F. Hill, and R. J. Adrian	Reynolds number scaling of flow in a Rushton turbine stirred tank: Part II—Eigen-decomposition of fluctuation—*Chemical Engineering Science* (submitted)	Aug. 2003